High-Frequency Resonance Suppression Based on Unified MMC High-Frequency Impedance Model

Xu, Zigao; Li, Binbin; Wang, Xiongfei; Blaabjerg, Frede; Xu, Dianguo

Published in:
IEEE Transactions on Power Electronics

DOI (link to publication from Publisher):
10.1109/TPEL.2022.3194885

Publication date:
2022

Document Version
Accepted author manuscript, peer reviewed version

High-Frequency Resonance Suppression Based on Unified MMC High-Frequency Impedance Model

Zigao Xu, *Student Member*, *IEEE*, Binbin Li, *Senior Member*, *IEEE*, Xiongfei Wang, *Senior Member, IEEE*, Frede Blaabjerg, *Fellow, IEEE* and Dianguo Xu, *Fellow*, *IEEE*

***Abstract*—High-frequency resonance (HFR) in the modular multilevel converter (MMC) has been reported in recent years frequently, yet, existing focuses on HFR are limited to the specific control strategy or grid condition, from which the conclusion may be not applicable if the control or grid changes. In this paper, a unified MMC high-frequency impedance model (UHFIM) is proposed to fill this gap. By changing the gain of the model, UHFIM can reflect the high-frequency characteristics of the MMC under different control strategies in a unified form, which provides a theoretical basis for the general HFR suppression method. Analysis based on UHFIM reveals the worst cases of the HFR risk and the constraint of low-pass filter (LPF) order on the convergence of MMC high-frequency damping. In order to suppress HFR, this paper proposes a joint design method for LPF and passive damper, which can completely remove the HFR risk from the entire high-frequency range without sacrificing too much dynamic performance of MMC, and it works no matter how the grid impedance varies. Besides, in the case that the damper cannot be installed, an alternative HFR suppression method based on delay time adjustment is also developed. Finally, the proposed unified model and the HFR suppression methods have been verified by simulation and experimental results.**

***Index Terms*—unified impedance model, low-pass filter (LPF) design, high-frequency resonance (HFR), damper.**

I. INTRODUCTION

Compared with the traditional generator with large inertia and low bandwidth, the power electronic converter has faster control speed and is easier to interact with passive components such as filter, series/parallel compensation and parasitic parameters of the power line, causing high-frequency resonance (HFR) with hundreds or even thousands of Hertz [1]. HFR issues have received early attention in the two-level converter based renewable energy generation where the phase lag of the delay time and the resonant peak of LCL filter or parallel compensation capacitor may excite oscillation in the high-frequency range [2]. This HFR is easily suppressed by the active resistance control as the damping can be accurately configured near the LCL resonant peak according to filter and compensation capacitor parameters known in advance [3], [4]. Besides, HFR can also be addressed by reducing the delay time of the two-level converter's modulation since the smaller delay time can improve the phase margin [5]. However, in the field of MMC-HVDC, HFR issues are more severe compared to the two-level converter. On the one hand, the MMC has a complex control structure that consists of a longer communication link and more signals. As a result, the delay time of an MMC control system can reach hundreds of microseconds which is much greater than that of two-level converter and cannot be significantly reduced only by modifying the modulation [8] (e.g., the delay time of LuXi project even exceeds 500μs [9]). On the other hand, the MMC is unnecessary to equip an extra filter due to high quality of its waveform. Therefore, HFR in MMC is caused by the interaction with the grid impedance instead of the LCL filter. Numerous resonant frequencies introduced by the power line are difficult to predict due to the dispersion of parasitic parameters. Moreover, the resonant frequency would be varied if some lines are cut off. These differences from the two-level converter bring great challenges to the HFR suppression of MMC and lead to the occurrence of HFR in MMC-HVDC projects. In [9], an oscillation at the frequency of 1270Hz is reported in LuXi project, where the oscillation voltage reached 68.9kV. Ref. [10] shows that 1810Hz and 700Hz high-frequency oscillations occurred successively in YuE project. And [11] discloses that a 1550Hz HFR had appeared in Zhangbei HVDC grid.

To solve HFR issues, the influence of time delay on HFR is studied in [6] based on MMC state space model. However, Pade approximation has to be used to model the time delay as the state, bringing errors to the high-frequency analysis [7]. Zou et al. [9] studied the HFR mechanism of the MMC based on the impedance analysis, and pointed out that the ac voltage feedforward link is the main cause for introducing high-frequency negative damping and leading to oscillations. In [10], a round link is inserted into the voltage feedforward link to block voltage perturbations and thus the negative damping caused by the voltage feedforward can be completely removed. However, further analysis shows that the ac current control also causes non-negligible negative damping in the high-frequency range which cannot be suppressed by only dealing with the voltage feedforward. To suppress the HFR risk caused by current control and voltage feedforward at the same time, Li et al. [12] adopts active resistance control to regulate the MMC damping in the high-frequency range. In [13], the active resistance of [12] is modified as the active impedance, which can be designed to offset the negative damping caused by both ac current control and ac voltage feedforward. On the other hand, low-pass filter (LPF) has a wider frequency range to weaken the negative damping of voltage feedforward and current control, and it is easier to implement. Zhu et al. [15] suppresses HFR by using the ac voltage and current LPFs, but the design process is just based on trial-and-error way. Ji et al. [16] uses a genetic algorithm to obtain filter parameters, whereas the genetic algorithm cannot reveal the design details. Although these methods successfully suppressed the HFR in a

This work was supported by National Natural Science Foundation of China under Grant 51720105008. (Corresponding author: Binbin Li)

Z. Xu, B. Li and D. Xu are with the School of Electrical Engineering and Automation, Harbin Institute of Technology, Harbin 150001, China (e-mail: orangesonhigh@163.com; libinbin@hit.edu.cn; xudiang@hit.edu.cn).

X. Wang and F. Blaabjerg are with the Department of Energy Technology, Aalborg University, 9220 Aalborg, Denmark (e-mail: xwa@energy.aau.dk; fbl@et.aau.dk).

certain grid condition, under the large delay time of MMC, the controller is difficult to act as an ideal resistance or eliminate the negative damping in the entire high-frequency range. As a result, if the grid impedance changes, the system may still face new HFR risk. Concerned about the uncertainty of MMC HFR frequency caused by changing grid impedance, an adaptive suppression strategy is reported in [14] where the frequency of HFR is extracted by the Fast Fourier Transform (FFT), and a notch filter is used to suppress this frequency component. This method, however, cannot take care of the case that multiple resonant frequencies appear at the same time and the notch filter may attenuate one oscillation while arise another.

In order to cope with the changing grid impedance, it is reasonable to use passive damper. The well-designed damper will be technically, economically mature and efficient [9]. Sun et al. [17] gives several damper structures suitable for the power system, which ensures that the resistance only acts on the high-frequency range by using series or parallel resonant branch, avoiding the power loss caused by low-frequency current flowing through the resistor. Ji et al. [18] deftly integrates the damper into the MMC arm inductors to reduce the voltage stress of passive elements. Compared with the active method or LPF which only weakens but does not remove the negative damping, the damper is able to directly correct the negative damping to positive, and thus it is considered to be a competitive way to completely eliminate the HFR risk. However, existing efforts mainly focus on the topology of the filter, while how to select the resistance of passive damper has not been discussed in detail.

It is found that the existing work on MMC HFR issues only pay attention to one specific control strategy while differences in the contribution of various MMC controls to the HFR were not discussed. As to HFR suppression, on the other hand, how much damping the passive damper needs to provide depends on the value of MMC negative damping. While the negative damping can be suppressed by LPF, it may also reduce its control bandwidth. The relationship among LPF, passive damper, and the MMC dynamic performance is still not clear. This paper focuses on the general solution of HFR issues, from modeling, analysis to HFR suppression method. The main contributions can be summarized as follows:

(a) A unified high-frequency impedance model (UHFIM) is proposed, which can reflect the high-frequency characteristics of MMC under various control strategies in a unified form, providing an effective and concise mathematical tool for a general HFR analysis.

(b) The quantitative relationship among LPF bandwidth, MMC negative damping and control bandwidth is analyzed based on UHFIM, by which a joint design method for LPF and damper is developed.

Different from the existing literature that only discusses HFR under a single control strategy, this paper, in section II, fully considering various MMC control strategies, establishes high-frequency impedances based on harmonic state space (HSS) to compare the effects of different controls on the HFR. Based on these impedances, in section III, the UHFIM is proposed, which reveals that the power control mode would be the worst case of HFR while the ac voltage control is the opposite. It also reveals the constraint of the LPF order the on MMC damping convergence. In section IV, instead of focusing on LPF or damper alone, the joint design for LPF and passive damper is developed based on UHFIM, which not only eliminates the HFR risk of the entire high-frequency range even after the grid impedance changes, but also reduces the impact of LPF on the MMC dynamic performance as much as possible. Besides, in the case that the damper cannot be installed, a HFR suppression method based on delay time adjustment and LPF design is also proposed as an alternative. Finally, the proposed model and the HFR suppression methods are demonstrated and verified by simulation and experimental results in section V, followed by the conclusion in section VI.

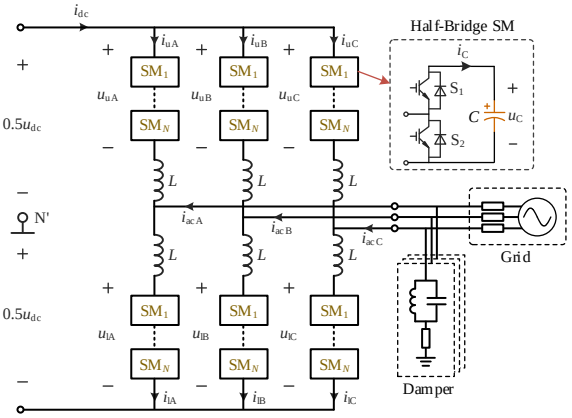

Fig. 1. Circuit of MMC.

II. MMC Impedance in High-Frequency Range

A. HSS Based MMC High-Frequency Impedance Modeling

Transforming MMC circuit shown in Fig. 1 into the differential- and common- mode form, the complete MMC linearized model is obtained based on HSS theory (detailed modeling process can be found in [19]), that is

$$\begin{bmatrix}\tilde{\mathbf{u}}_{\rm dc}\\ \tilde{\mathbf{u}}_{\rm ac}\end{bmatrix}=\begin{bmatrix}\mathbf{K}_{\rm icm1} & \mathbf{K}_{\rm i1}\\ \mathbf{K}_{\rm icm2} & \mathbf{K}_{\rm i2}\end{bmatrix}\begin{bmatrix}\tilde{\mathbf{i}}_{\rm cm}\\ \tilde{\mathbf{i}}_{\rm ac}^{\pm}\end{bmatrix}+\begin{bmatrix}\mathbf{K}_{\rm mcm1} & \mathbf{K}_{\rm mdm1}\\ \mathbf{K}_{\rm mcm2} & \mathbf{K}_{\rm mdm2}\end{bmatrix}\begin{bmatrix}\tilde{\mathbf{m}}_{\rm cm}\\ \tilde{\mathbf{m}}_{\rm dm}\end{bmatrix} \tag{1a}$$

where

$$\begin{cases}\mathbf{K}_{\rm icm1}=2L\mathbf{S}+\dfrac{2N}{C}\mathbf{m}_{\rm cm}\mathbf{S}^{-1}\mathbf{m}_{\rm cm}+\dfrac{2N}{C}\mathbf{m}_{\rm dm}\mathbf{S}^{-1}\mathbf{m}_{\rm dm}\\ \mathbf{K}_{\rm i1}=\dfrac{N}{C}\mathbf{m}_{\rm cm}\mathbf{S}^{-1}\mathbf{m}_{\rm dm}+\dfrac{N}{C}\mathbf{m}_{\rm dm}\mathbf{S}^{-1}\mathbf{m}_{\rm cm}\\ \mathbf{K}_{\rm icm2}=\dfrac{N}{C}\mathbf{m}_{\rm dm}\mathbf{S}^{-1}\mathbf{m}_{\rm cm}+\dfrac{N}{C}\mathbf{m}_{\rm cm}\mathbf{S}^{-1}\mathbf{m}_{\rm dm}\\ \mathbf{K}_{\rm i2}=\dfrac{L}{2}\mathbf{S}+\dfrac{N}{2C}\mathbf{m}_{\rm dm}\mathbf{S}^{-1}\mathbf{m}_{\rm dm}+\dfrac{N}{2C}\mathbf{m}_{\rm cm}\mathbf{S}^{-1}\mathbf{m}_{\rm cm}\end{cases} \tag{1b}$$

$$\begin{cases}\mathbf{K}_{\rm mcm1}=\dfrac{2N}{C}\mathbf{m}_{\rm cm}\mathbf{S}^{-1}\mathbf{i}_{\rm cm}+\dfrac{N}{C}\mathbf{m}_{\rm dm}\mathbf{S}^{-1}\mathbf{i}_{\rm ac}^{\pm}+2N\mathbf{u}_{\rm Ccm}\\ \mathbf{K}_{\rm mdm1}=\dfrac{N}{C}\mathbf{m}_{\rm cm}\mathbf{S}^{-1}\mathbf{i}_{\rm ac}^{\pm}+\dfrac{2N}{C}\mathbf{m}_{\rm dm}\mathbf{S}^{-1}\mathbf{i}_{\rm cm}+2N\mathbf{u}_{\rm Cdm}\\ \mathbf{K}_{\rm mcm2}=\dfrac{N}{C}\mathbf{m}_{\rm dm}\mathbf{S}^{-1}\mathbf{i}_{\rm cm}+\dfrac{N}{2C}\mathbf{m}_{\rm cm}\mathbf{S}^{-1}\mathbf{i}_{\rm ac}^{\pm}+N\mathbf{u}_{\rm Cdm}\\ \mathbf{K}_{\rm mdm2}=\dfrac{N}{2C}\mathbf{m}_{\rm dm}\mathbf{S}^{-1}\mathbf{i}_{\rm ac}^{\pm}+\dfrac{N}{C}\mathbf{m}_{\rm cm}\mathbf{S}^{-1}\mathbf{i}_{\rm cm}+N\mathbf{u}_{\rm Ccm}\end{cases} \tag{1c}$$

$$\mathbf{S}=\mathrm{diag}\left[\cdots,\ \mathrm{j}(\omega-\omega_1),\ \mathrm{j}\omega,\ \mathrm{j}(\omega+\omega_1),\ \cdots\right]. \tag{1d}$$

In (1), C, L and N denote the capacitance, inductance, and the sub-module number of the MMC. The bold variables with tilde

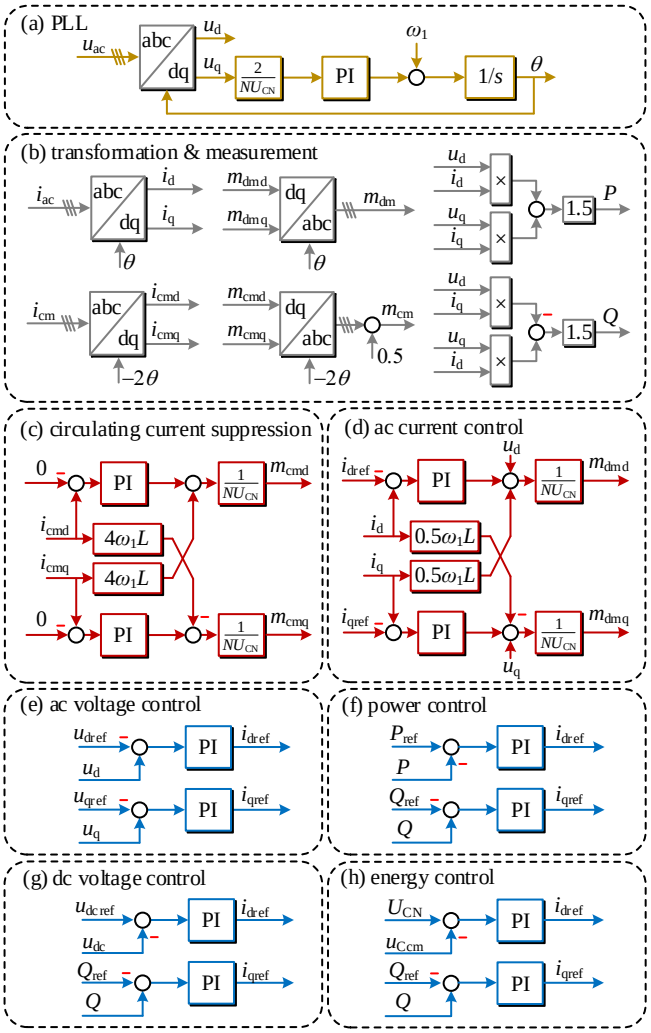

Fig. 2. MMC control strategies.

hat "~" denote the perturbation vectors, and others are steady components expressed by the Toeplitz matrix. $\tilde{\mathbf{u}}_{dc}$ and $\tilde{\mathbf{u}}_{ac}$ are terminal voltages of MMC ac and dc sides, respectively. $\tilde{\mathbf{u}}_C$ is the capacitor voltage, and $\tilde{\mathbf{m}}$ is the modulation index, where the subscript "cm" and "dm" indicate common- and differential-mode components of variables, respectively. Taking the inflow of MMC from the grid as the reference direction, the circulating current and ac current are expressed as $\tilde{\mathbf{i}}_{cm}$ and $\tilde{\mathbf{i}}_{ac}^{\pm}$, in which "±" represents that only positive- or negative- sequence components can be found in the ac current due to the three-phase three-wire configuration.

The HSS model (1) is detailed but complex as it fully reflects the MMC harmonics coupling features. Fortunately, [20] has proven that these couplings mainly act on the low-frequency range without affecting the MMC high-frequency impedance due to the suppression effect of the inductor and capacitor on high-frequency perturbations. Ignoring the coupling frequency in (1d), such as $\omega\pm\omega_1$, $\omega\pm\omega_2$, etc., and considering $\mathbf{S}^{-1}$ tends to 0 in the high-frequency range, Eq. (1a) is simplified as

$$\begin{cases} \tilde{u}_{dc} = \mathrm{j}2\omega L\tilde{i}_{cm} + 2NU_{Ccm}\tilde{m}_{cm} \\ \tilde{u}_{ac} = \mathrm{j}\omega\dfrac{L}{2}\tilde{i}_{ac}^{\pm} + NU_{Ccm}\tilde{m}_{dm} \end{cases} \tag{2}$$

where variables change from the vector to the scalar since coupling items are removed. U_{Ccm} denotes the dc component of the capacitor voltage. When the MMC operates without control, $\tilde{m}_{cm}$ and $\tilde{m}_{dm}$ equal to 0, and then MMC high-frequency impedances can be derived as

$$Z_{ac} = \frac{\tilde{u}_{ac}}{\tilde{i}_{ac}^{\pm}} = \mathrm{j}\omega\frac{L}{2} \tag{3a}$$

$$Z_{dc} = \frac{\tilde{u}_{dc}}{3\tilde{i}_{cm}^{0}} = \mathrm{j}\omega\frac{2L}{3}. \tag{3b}$$

Eq. (3) shows that the open-loop MMC acts as a pure inductor in the high-frequency range (ignoring the arms parasitic resistance), both on ac and dc side. In this case, the MMC impedance does not contain negative damping, and thus has no risk of HFR.

B. High-Frequency Impedance with Closed-loop Control

This part aims to derive the MMC high-frequency impedance with fully considering MMC control strategies in the industry, including phase-locked loop (PLL), circulating current suppression, ac current inner-loop control, and outer loops for controlling the ac voltage, the power, the dc voltage and the storage energy, respectively, as shown in Fig. 2.

(i) PLL

Observing Fig. 2(a), an integral link can be founded in the structure of the PLL, which strongly attenuates high-frequency perturbations. Besides, low PLL bandwidth is always adopted to avoid the sub-synchronous oscillation. Therefore, the impact of PLL on the high-frequency impedance is ignored in almost all of the existing work [9]-[16], and so do in this paper.

(ii) Circulating Current Suppression

Fig. 2(c) presents a circulating current suppression strategy based on a double line-frequency synchronous reference frame, where the gain $1/(NU_{CN})$ is used for normalization and U_{CN} denotes the rated voltage of each sub module. As this control acts only on the dq components of the circulating current, the zero-sequence component which flows to the dc side is out of control, so that it does not have any effect on the MMC dc impedance. As a result, the MMC dc impedance would always behave as a pure inductor without any negative damping even under the closed-loop control. This also explains why the HFR in MMC dc side is seldom reported.

(iii) Ac Current Control

The HSS expression of the modulation index can be derived from the ac current control shown in Fig. 2(d) (details are shown in Appendix), we have

$$\begin{aligned} \tilde{\mathbf{m}}_{dm} = \frac{1}{NU_{CN}}\Big\{ & -\mathbf{T}_{d-}K_{iac}\tilde{\mathbf{i}}_{dref} - \mathbf{T}_{q-}K_{iac}\tilde{\mathbf{i}}_{qref} + \mathbf{E}_{\pm}^{s}\mathrm{e}^{-\mathrm{j}\omega T_d}\tilde{\mathbf{u}}_{ac} \\ & + \left[K_{iac}\mathbf{E}_{\pm}^{s} + \mathrm{j}\left(-\mathbf{E}_{+}^{s} + \mathbf{E}_{-}^{s}\right)\omega_1 L_{eq}\right]\mathrm{e}^{-\mathrm{j}\omega T_d}\tilde{\mathbf{i}}_{ac}\Big\} \end{aligned} \tag{4}$$

where L_{eq} is the equivalent ac inductance and equals $L/2$. $\mathbf{T}_{dq+}$ and $\mathbf{T}_{dq-}$ represent the Park and the inverse Park transformations, respectively. $\mathbf{E}_{+}^{s}$, $\mathbf{E}_{-}^{s}$ and $\mathbf{E}_{\pm}^{s}$ ($\mathbf{E}_{\pm}^{s}=\mathbf{E}_{+}^{s}+\mathbf{E}_{-}^{s}$) are sequence extraction matrixes, where $\mathbf{E}_{+}^{s}$ equals 1 and 0 for the positive- and the negative- sequence signals, respectively, and $\mathbf{E}_{-}^{s}$ is just the opposite [19]. K_{iac} denotes the proportional gain of PI controller, and the influence of the integral link can be ignored in the high-frequency range. T_d is the delay of the control system. The positive-sequence impedance is derived in

this paper as an example, and the analysis of the negative-sequence impedance is similar. Substituting $\mathbf{E}^s_{\pm}=\mathbf{E}^s_{+}=1$ into (4) and removing the coupling frequency leads to

$$\tilde{m}_{\mathrm{dm}}=\frac{1}{NU_{\mathrm{CN}}}\left[\mathrm{e}^{-\mathrm{j}\omega T_{\mathrm{d}}}\tilde{u}_{\mathrm{ac}}+\left(K_{\mathrm{iac}}-\mathrm{j}\omega_1 L_{\mathrm{eq}}\right)\mathrm{e}^{-\mathrm{j}\omega T_{\mathrm{d}}}\tilde{i}_{\mathrm{ac}}\right] \tag{5}$$

where reference signals are omitted because the outer loop has not been added at this step. Substituting (5) into (2), the MMC high-frequency impedance in ac side is obtained as

$$Z_{\mathrm{ac}}=\mathrm{j}\omega L_{\mathrm{eq}}+\frac{K_{\mathrm{iac}}-\mathrm{j}\omega_1 L_{\mathrm{eq}}+\mathrm{j}\omega L_{\mathrm{eq}}}{\mathrm{e}^{\mathrm{j}\omega T_{\mathrm{d}}}-1}. \tag{6}$$

Noted that U_{Ccm} in (2) would be close to the rated capacitor voltage U_{CN} in (5) during MMC normal operation, so these two terms are approximately cancelled and removed from (6). Eq. (6) shows that the ac current control will introduce an additional item to the MMC high-frequency impedance in ac side, which is related to the current gain, voltage feedforward, delay time and dq decoupling link.

(iv) Ac Voltage Control

The ac voltage control is commonly applied in wind power collection station or islanded grid, and the control strategy is shown in Fig. 2(e). The controller generates the reference signal of the current inner loop according to the ac voltage error:

$$\begin{cases}\tilde{\mathbf{i}}_{\mathrm{dref}}=-K_{\mathrm{uac}}\left(\tilde{\mathbf{u}}_{\mathrm{dref}}-\mathbf{T}_{\mathrm{d+}}\tilde{\mathbf{u}}_{\mathrm{ac}}\right)\\ \tilde{\mathbf{i}}_{\mathrm{qref}}=-K_{\mathrm{uac}}\left(\tilde{\mathbf{u}}_{\mathrm{qref}}-\mathbf{T}_{\mathrm{q+}}\tilde{\mathbf{u}}_{\mathrm{ac}}\right)\end{cases} \tag{7}$$

where K_{uac} is proportional gain of the controller. Connecting (7) with (4) and ignoring the couplings, we have

$$\tilde{m}_{\mathrm{dm}}=\frac{1}{NU_{\mathrm{CN}}}\left[\left(1-K_{\mathrm{iac}}K_{\mathrm{uac}}\right)\mathrm{e}^{-\mathrm{j}\omega T_{\mathrm{d}}}\tilde{u}_{\mathrm{ac}}+\left(K_{\mathrm{iac}}-\mathrm{j}\omega_1 L_{\mathrm{eq}}\right)\mathrm{e}^{-\mathrm{j}\omega T_{\mathrm{d}}}\tilde{i}_{\mathrm{ac}}\right]. \tag{8}$$

Substituting (8) into (2), the MMC high-frequency impedance under the ac voltage control can be derived as

$$Z_{\mathrm{ac}}=\mathrm{j}\omega L_{\mathrm{eq}}+\frac{\dfrac{K_{\mathrm{iac}}-\mathrm{j}\omega_1 L_{\mathrm{eq}}}{1-K_{\mathrm{iac}}K_{\mathrm{uac}}}+\mathrm{j}\omega L_{\mathrm{eq}}}{\dfrac{\mathrm{e}^{\mathrm{j}\omega T_{\mathrm{d}}}}{1-K_{\mathrm{iac}}K_{\mathrm{uac}}}-1}. \tag{9}$$

Compared to the ac current control, Eq. (9) shows that the ac voltage control will introduce an additional gain $K_{\mathrm{iac}}K_{\mathrm{uac}}$ into the MMC high-frequency ac impedance.

(v) Power Control

Fig. 2(f) presents the block diagram of the power control. The active and the reactive power can be calculated by ac voltage and current, as shown in Fig. 2(b), and then input to the controllers to generate the current reference:

$$\begin{cases}\tilde{\mathbf{i}}_{\mathrm{dref}}=K_{\mathrm{PQ}}\left[\tilde{\mathbf{P}}_{\mathrm{ref}}-1.5\mathbf{u}_{\mathrm{d}}\mathbf{T}_{\mathrm{d+}}\tilde{\mathbf{i}}_{\mathrm{ac}}-1.5\left(\mathbf{i}_{\mathrm{d}}\mathbf{T}_{\mathrm{d+}}+\mathbf{i}_{\mathrm{q}}\mathbf{T}_{\mathrm{q+}}\right)\tilde{\mathbf{u}}_{\mathrm{ac}}\right]\\ \tilde{\mathbf{i}}_{\mathrm{qref}}=-K_{\mathrm{PQ}}\left[\tilde{\mathbf{Q}}_{\mathrm{ref}}+1.5\mathbf{u}_{\mathrm{d}}\mathbf{T}_{\mathrm{q+}}\tilde{\mathbf{i}}_{\mathrm{ac}}-1.5\left(-\mathbf{i}_{\mathrm{q}}\mathbf{T}_{\mathrm{d+}}+\mathbf{i}_{\mathrm{d}}\mathbf{T}_{\mathrm{q+}}\right)\tilde{\mathbf{u}}_{\mathrm{ac}}\right]\end{cases}. \tag{10}$$

Similarly, the modulation index and the ac impedance are

$$\tilde{m}_{\mathrm{dm}}=\frac{1}{NU_{\mathrm{CN}}}\left[\mathrm{e}^{-\mathrm{j}\omega T_{\mathrm{d}}}\tilde{u}_{\mathrm{ac}}+\left(K_{\mathrm{iac}}-\mathrm{j}\omega_1 L_{\mathrm{eq}}+1.5K_{\mathrm{iac}}K_{\mathrm{PQ}}U_{\mathrm{d}}\right)\mathrm{e}^{-\mathrm{j}\omega T_{\mathrm{d}}}\tilde{i}_{\mathrm{ac}}\right] \tag{11}$$

$$Z_{\mathrm{ac}}=\mathrm{j}\omega L_{\mathrm{eq}}+\frac{K_{\mathrm{iac}}-\mathrm{j}\omega_1 L_{\mathrm{eq}}+1.5K_{\mathrm{iac}}K_{\mathrm{PQ}}U_{\mathrm{d}}+\mathrm{j}\omega L_{\mathrm{eq}}}{\mathrm{e}^{\mathrm{j}\omega T_{\mathrm{d}}}-1} \tag{12}$$

where U_{d} and I_{d} are amplitudes of the d-axis steady-state voltage and current, respectively. Obviously, the impedance becomes more complicated as it is not only affected by the gain of the inner and outer loops, but also affected by the voltage and current of MMC.

(vi) Dc Voltage Control

DC voltage control is implemented by adjusting the d-axis current, and the q-axis current is usually connected to the reactive power controller for reactive compensation, as shown in Fig. 2(g), which leads to

$$\begin{cases}\tilde{\mathbf{i}}_{\mathrm{dref}}=K_{\mathrm{udc}}\left(\tilde{\mathbf{u}}_{\mathrm{dcref}}-\tilde{\mathbf{u}}_{\mathrm{dc}}\right)\\ \tilde{\mathbf{i}}_{\mathrm{qref}}=-K_{\mathrm{PQ}}\left[\tilde{\mathbf{Q}}_{\mathrm{ref}}+1.5\mathbf{u}_{\mathrm{d}}\mathbf{T}_{\mathrm{q+}}\tilde{\mathbf{i}}_{\mathrm{ac}}-1.5\left(-\mathbf{i}_{\mathrm{q}}\mathbf{T}_{\mathrm{d+}}+\mathbf{i}_{\mathrm{d}}\mathbf{T}_{\mathrm{q+}}\right)\tilde{\mathbf{u}}_{\mathrm{ac}}\right]\end{cases}. \tag{13}$$

Due to the attenuation effect of MMC capacitors and inductors, high-frequency perturbations on ac side are difficult to penetrate MMC into dc side [20], thereby $\tilde{\mathbf{u}}_{\mathrm{dc}}$ can be removed from (13). Then we have

$$\begin{aligned}\tilde{m}_{\mathrm{dm}}=\frac{1}{NU_{\mathrm{CN}}}&\left\{\left[1-0.75K_{\mathrm{iac}}K_{\mathrm{PQ}}\left(I_{\mathrm{d}}-\mathrm{j}I_{\mathrm{q}}\right)\right]\mathrm{e}^{-\mathrm{j}\omega T_{\mathrm{d}}}\tilde{u}_{\mathrm{ac}}\right.\\ &\left.+\left(K_{\mathrm{iac}}-\mathrm{j}\omega_1 L_{\mathrm{eq}}+0.75K_{\mathrm{iac}}K_{\mathrm{PQ}}U_{\mathrm{d}}\right)\mathrm{e}^{-\mathrm{j}\omega T_{\mathrm{d}}}\tilde{i}_{\mathrm{ac}}\right\}\end{aligned} \tag{14}$$

$$Z_{\mathrm{ac}}=\mathrm{j}\omega L_{\mathrm{eq}}+\frac{\dfrac{K_{\mathrm{iac}}-\mathrm{j}\omega_1 L_{\mathrm{eq}}+0.75K_{\mathrm{iac}}K_{\mathrm{PQ}}U_{\mathrm{d}}}{1-0.75K_{\mathrm{iac}}K_{\mathrm{PQ}}\left(I_{\mathrm{d}}-\mathrm{j}I_{\mathrm{q}}\right)}+\mathrm{j}\omega L_{\mathrm{eq}}}{\dfrac{\mathrm{e}^{\mathrm{j}\omega T_{\mathrm{d}}}}{1-0.75K_{\mathrm{iac}}K_{\mathrm{PQ}}\left(I_{\mathrm{d}}-\mathrm{j}I_{\mathrm{q}}\right)}-1}. \tag{15}$$

It is seen from (15) that although the dc voltage controller does not affect the MMC ac high-frequency impedance, the existence of reactive power control still makes the impedance contain the steady-state voltage and current.

(vii) Energy Control

When we need to control the storage energy of MMC sub modules, the outer loop shown in Fig. 2(h) can be adopted [21], [22], where the d-axis current is used to adjust the capacitor voltage to the rated value, and the q-axis current is used for reactive compensation. In this case, the perturbation of the capacitor voltage can also, similar to $\tilde{\mathbf{u}}_{\mathrm{dc}}$ in (13), be ignored considering the attenuation effect of sub-module capacitor on the high-frequency components. And reactive power control is still the only outer loop that affects the MMC ac impedance, so the impedance would be the same as (15).

III. Unified MMC High-Frequency Impedance Model

Observing (5), (8), (11) and (14), it is found that the reason why the control strategies affect the MMC high-frequency impedance is that they introduce the signal path of ac voltage and current into the modulation index. Different voltage and current gains lead to different high-frequency impedance of MMC. It is because the impedance model is essentially a transfer function from terminal current to terminal voltage, as a result, only the control that can affect the high-frequency voltage and current gain shapes the MMC high-frequency impedance. This paper uniformly expresses the voltage and current gains with G_{i} and G_{u} respectively, so that the unified MMC high-frequency impedance model (UHFIM) can be obtained, which is

$$Z_{ac} = j\omega L_{eq} + \frac{\frac{|G_i|}{|G_u|}e^{j\theta_2} + j\omega L_{eq}}{\frac{e^{j\theta_1}}{|G_u|} - 1} \quad (16)$$

where $\theta_1=T_d\omega-\varphi_u$, $\theta_2=\varphi_i-\varphi_u$; $|G_i|$, $|G_u|$ and φ_i, φ_u denote the amplitude and the phase of the current and voltage gain, respectively. The proposed model can analyze HFR issues under various control scenarios in a unified mathematical form. For different scenarios, the MMC high-frequency impedance can be easily acquired by substituting the gain of Table I into (16). Moreover, for other control strategies not mentioned herein, the impedance model can also be organized into the form of (16) by extracting voltage and current gain.

TABLE I. UHFIM GAINS UNDER DIFFERENT CONTROL STRATEGIES

Stradegies	Gains
ac current ctrl.	$G_i = K_{iac} - j\omega_1 L_{eq}$ $G_u = 1$
ac voltage ctrl.	$G_i = K_{iac} - j\omega_1 L_{eq}$ $G_u = 1 - K_{iac}K_{uac}$
power ctrl.	$G_i = K_{iac} - j\omega_1 L_{eq} + 1.5K_{iac}K_{PQ}U_d$ $G_u = 1$
dc voltage ctrl. (or energy ctrl.)	$G_i = K_{iac} - j\omega_1 L_{eq} + 0.75K_{iac}K_{PQ}U_d$ $G_u = 1 - 0.75K_{iac}K_{PQ}(I_d - jI_q)$

According to impedance criteria, instability occurs when the phase angle difference at the impedance intersection of the two subsystems exceeds 180°. This criterion can be expressed equivalently that when the reactance of two subsystems is capacitive and inductive respectively at the intersection with the negative net damping, the system will be unstable [23]. Based on UHFIM, this section will discuss the frequency characteristics of both MMC damping and reactance to provide the theoretical basis for subsequent HFR suppression.

A. High-Frequency Damping

High-frequency negative damping is the culprit of HFR, which can be studied by abstracting the real part from (16):

$$\mathrm{Re}(Z_{ac}) = \frac{|G_i|\left[\cos(\theta_1-\theta_2) - |G_u|\cos\theta_2\right] + |G_u|\omega L_{eq}\sin\theta_1}{(\cos\theta_1 - |G_u|)^2 + (\sin\theta_1)^2}. \quad (17)$$

Observing (17), it can be found that the MMC high-frequency damping alternates between positive and negative periodically with the increase of frequency, and the negative damping will tend to infinity when the condition of $\cos\theta_1=|G_u|=1$ is met, which brings serious hidden danger of the HFR. The blue curve in Fig. 3 shows the MMC high-frequency impedance with a delay of 500μs, where the ac current control with K_{iac}=50 is adopted. In this case, the voltage gain G_u always equals 1 due to the unit voltage feedforward, and thus there is an obvious resonant peak at the position that $\cos\theta_1=1$ holds (i.e., $f=n/T_d$, $n\in\mathbf{N}^+$, such as 2kHz, 4kHz, 6kHz, etc.). Negative damping occurs in the frequency range where the real part is less than zero as shown in Fig. 3(b), and it corresponds to the part whose phase angle exceeds 90° in Fig. 3(a). In order to weaken the negative damping, the amplitude of G_u must be suppressed. The

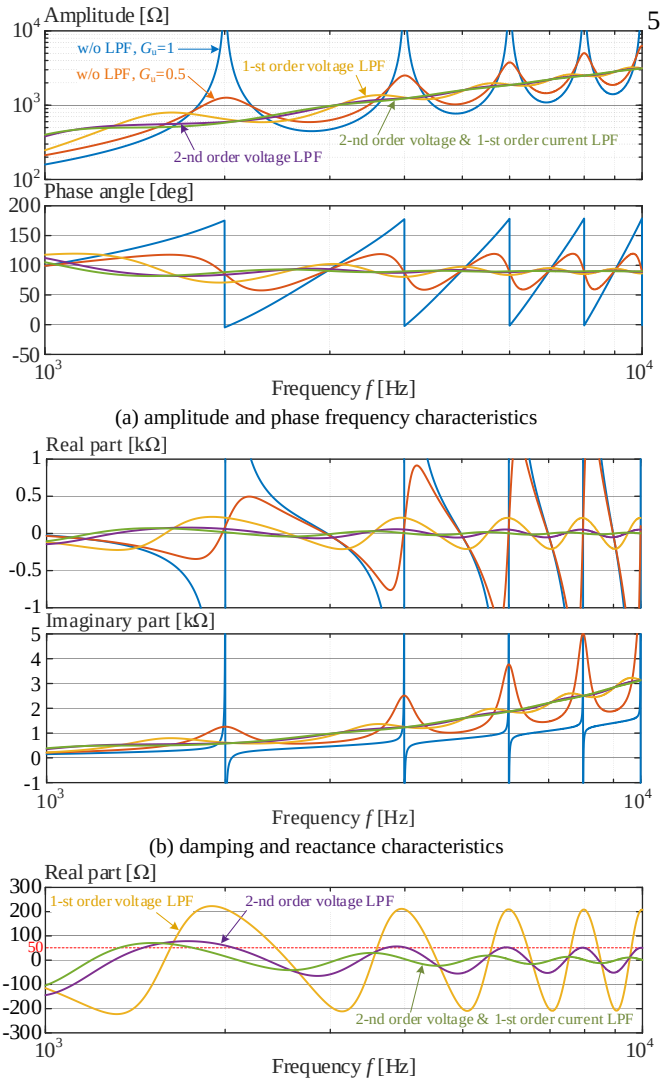

(a) amplitude and phase frequency characteristics

(b) damping and reactance characteristics

(c) zoom-in plot of the MMC damping

Fig. 3. MMC high-frequency impedance (T_d=500μs, L=100mH).

orange curve denotes the MMC impedance with a smaller constant feedforward gain (G_u=0.5). This method reduces the resonant peak to a certain extent as shown in Fig. 3(a), but Fig. 3(b) reveals that the MMC negative damping will gradually diverge with the increase of frequency. The root cause of this phenomenon is that the numerator of the MMC high-frequency damping includes an item proportional to the angle frequency ω, as shown in (17). Therefore, to avoid the divergence of MMC negative damping, an LPF has to be inserted into the voltage path. Noted that the first-order LPF provides the attenuation rate of -20dB/dec, which just offsets the ω in the numerator to make it no longer increase. Only the second- or higher order LPF can ensure that this item converges to 0. The yellow and purple curves in Fig. 3 indicate the impedance with the first and the second-order voltage LPF, respectively. The zoom-in plot Fig. 3(c) reflects that the damping is no longer diverged after adding these two kinds of voltage LPF, and it would be smaller with the second-order LPF. However, the purple curve does not attenuate to 0 because there is still one item in the numerator of (17), that is $|G_i|[\cos(\theta_1-\theta_2)-|G_u|\cos\theta_2]$. The amplitude of this item will approximate the current gain, which equals to 50 in this example and consistent with the purple curve in Fig. 3(c). Therefore, to ensure the further attenuation of negative damping, a first-order LPF needs to be added to the current path, as the green curve shown in Fig. 3(c).

Above discussion draws a conclusion that at least the second-order voltage LPF and the first-order current LPF are needed to make the MMC high-frequency negative damping converge to zero, so as to reduce the risk of HFR. This conclusion based on the UHFIM is universal in any cases.

B. High-Frequency Reactance

The MMC reactance in high-frequency range can be obtained by abstracting the imaginary part from (16):

$$\mathrm{Im}\left(Z_{\mathrm{ac}}\right)=\frac{\left|G_{\mathrm{i}}\right|\left[\sin\left(\theta_2-\theta_1\right)-\left|G_{\mathrm{u}}\right|\sin\theta_2\right]+\omega L_{\mathrm{eq}}\left[1-\left|G_{\mathrm{u}}\right|\cos\theta_1\right]}{\left(\cos\theta_1-\left|G_{\mathrm{u}}\right|\right)^2+\left(\sin\theta_1\right)^2}. \tag{18}$$

Comparing (17) and (18), it can be found that the numerator of MMC reactance has an additional term proportional to ω while independent of G_{u}, and thus it would not be affected by the voltage LPF. As a result, the MMC reactance will increase with the frequency, and the MMC high-frequency impedance is always inductive, as presented in Fig. 3(b). This means that the MMC will only face the HFR risk within the capacitive range of the connected load or grid impedance.

C. Discussion on Gains of Different Controls

The UHFIM can be used to compare the severity of different control strategies on the HFR. The larger G_{i} and the closer G_{u} to 1, the more serious the MMC negative damping in high-frequency range. It can be found from Table I that the power control would be the worst case where G_{i} is the largest in all strategies and G_{u} equals to 1, which means it will produce infinite negative damping. Ac current control also performs infinite negative damping due to its unit G_{u}, but it is slightly less than power control because it has small G_{i}. The G_{u} of dc and ac voltage controls is less than 1, so the negative damping is much less than that of power and ac current control. Among them, HFR risk of ac voltage control would be the smallest because this control always reduces G_{u} in the high-frequency range and has the smallest G_{i}. As a result, G_{u} and G_{i} under power control can be regarded as the upper limit of gains under other control strategies.

To get this upper limit, it is necessary to estimate the magnitude of the power control parameters. According to the control design for the first-order target with delay [24], the open-loop transfer function of the ac current control is

$$H_{\mathrm{idq}}\approx K_{\mathrm{iac}}\frac{1}{sL_{\mathrm{eq}}}\mathrm{e}^{-sT_{\mathrm{d}}}. \tag{19}$$

Let the magnitude of (19) be equal to 1 leading to

$$K_{\mathrm{iac}}=\omega_{\mathrm{ci}}L_{\mathrm{eq}}=\frac{\frac{\pi}{2}-\gamma_{\mathrm{i}}}{T_{\mathrm{d}}}L_{\mathrm{eq}} \tag{20}$$

where $\gamma_{\mathrm{i}}=\pi/2-\omega_{\mathrm{ci}}T_{\mathrm{d}}$ denotes the phase margin; ω_{ci} is the cut-off angle frequency of the ac current loop which can reflect the MMC control bandwidth. It is seen that for a given L_{eq}, the control bandwidth is completely determined by K_{iac}.

On the other hand, the transfer function of power loop can be written as

$$H_{\mathrm{PQ}}\approx K_{\mathrm{PQ}}\frac{3}{2}U_{\mathrm{d}}\frac{1}{\tau_{\mathrm{bi}}s+1} \tag{21}$$

where τ_{bi} is the time constant of ac current control and approximately equals to the reciprocal of ω_{ci}. It is generally believed that the bandwidth of the outer loop should be at least less than 1/10 of the current loop bandwidth to decouple the different control loops, and then we have

$$K_{\mathrm{PQ}}\frac{3}{2}U_{\mathrm{d}}\frac{1}{\tau_{\mathrm{bi}}\mathrm{j}\frac{\omega_{\mathrm{ci}}}{10}+1}\approx K_{\mathrm{PQ}}\frac{3}{2}U_{\mathrm{d}}=1\Rightarrow K_{\mathrm{PQ}}\approx\frac{1}{1.5U_{\mathrm{d}}}. \tag{22}$$

Based on (22), gains under power control are estimated as

$$\begin{cases}G_{\mathrm{i}}\approx 2K_{\mathrm{iac}}-\mathrm{j}\omega_1L_{\mathrm{eq}}=L_{\mathrm{eq}}\left(2\omega_{\mathrm{ci}}-\mathrm{j}\omega_1\right)\\ G_{\mathrm{u}}=1\end{cases}. \tag{23}$$

The MMC voltage and current gains under other control strategies would not exceed this limit. Eq. (23) reveals that the larger the control bandwidth and the MMC arm inductance, the larger G_{i} and their introduced negative damping.

One MMC station may change its control strategy due to adjustments in power grid planning. HFR suppression design directly for the worst case would be conservative but applicable to all kinds of control, which can avoid the inconvenience of replacing hardware (such as damper) after the control changes and can reduce the maintenance cost. If the change of control is not the concern, a more accurate analysis can be carried out by using the real voltage and current gains corresponding to the strategy in Table I instead of using the upper limit gains. The subsequent HFR suppression design process is same for both the upper limit gain and the real gain.

IV. HFR SUPPRESSION

Frequency characteristic analysis on MMC impedance has revealed the constraint relationship between the LPF order and convergence of the negative damping. Obviously, the lower the filter bandwidth, the stronger the negative damping suppression. However, the filter bandwidth cannot be reduced recklessly, otherwise it will deteriorate the MMC dynamic performance. In section III, it has been found that the LPF only weakens the negative damping, but cannot completely eliminate it. To remove the negative damping from the entire high-frequency range, the passive damper has to be used. This section will analyze, by using the UHFIM, the influence of LPF bandwidth on MMC negative damping, based on which a joint design method of LPF bandwidth and passive damper is proposed to completely eliminate the HFR without excessively affecting the dynamic performance of the system. Besides, an HFR suppression method based on delay time adjustment is also proposed as an alternative for the case that the damper cannot be installed.

A. Effect of LPF on High-Frequency Negative Damping and MMC Dynamic Performance

Consider following LPF transfer functions:

$$\begin{cases}G_{\mathrm{Fi}}\left(s\right)=\dfrac{1}{s/\left(2\pi f_{\mathrm{Fi}}\right)+1}\\ G_{\mathrm{Fu}}\left(s\right)=\dfrac{1}{\left[s/\left(2\pi f_{\mathrm{Fu}}\right)\right]^2+2\xi\left[s/\left(2\pi f_{\mathrm{Fu}}\right)\right]+1}\end{cases} \tag{24}$$

whose phase lags are

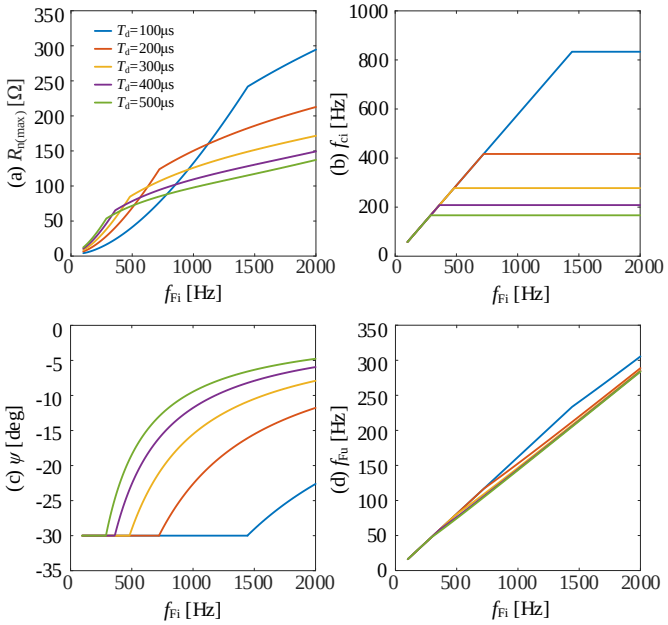

Fig. 4. Relationship among maximum negative damping, LPF bandwidth and dynamic performance under different delay times (L=100mH).

$$\begin{cases} \angle G_{\mathrm{Fi}}(\omega) = -\arctan\left[\omega/(2\pi f_{\mathrm{Fi}})\right] \\ \angle G_{\mathrm{Fu}}(\omega) = -\arctan\left\{\dfrac{2\xi\left[\omega/(2\pi f_{\mathrm{Fu}})\right]}{1-\left[\omega/(2\pi f_{\mathrm{Fu}})\right]^2}\right\} \end{cases} \tag{25}$$

where f_{Fi} and f_{Fu} indicate bandwidths of the current and voltage LPFs, respectively; ξ is the damping coefficient which is set as 0.707 in general. The influence of the LPF on dynamic performance is mainly reflected in the control bandwidth reduction. To avoid the degradation of dynamic performance as much as possible, the MMC control bandwidth f_{ci} (f_{ci}=ω_{ci}/2π) is set as the constant when reducing f_{Fi} initially. But as f_{Fi} decreases, the phase lag ψ introduced by current LPF at f_{ci} would reduce the phase margin. It is recommended that ψ should not be greater than 30° for ensuring stability of the control loop, and thereby the constraint of f_{Fi} can be obtained as

$$\angle G_{\mathrm{Fi}}(\omega_{ci}) \geq -30^\circ \Rightarrow f_{\mathrm{Fi}} \geq \frac{1}{12T_d \tan 30^\circ} = \frac{1}{4\sqrt{3}T_d}. \tag{26}$$

Similarly, the voltage LPF should also avoid introducing a phase lag exceeding 30° at f_{ci}/10, and thus f_{Fu} satisfies

$$f_{\mathrm{Fu}} \geq \frac{\omega_{ci}}{10}\frac{\xi+\sqrt{\xi^2+(\tan 30^\circ)^2}}{2\pi \tan 30^\circ} = \frac{\sqrt{3}+\sqrt{5}}{120\sqrt{2}T_d}. \tag{27}$$

When LPF bandwidth reaches the constraints of (26) and (27), further reducing f_{Fi} and f_{Fu} may lead to insufficient phase margin. To avoid this, f_{ci} needs to decrease, by turning down the controller parameter, in the same proportion as f_{Fi}, so that phase lag of current LPF at f_{ci} can remain constant. Likewise, f_{Fu} should also decrease in the same proportion as f_{ci}/10. As a result, by adding the LPF, voltage and current gains in (23) can be expressed as

$$\begin{cases} G_i = L_{eq}(2k\omega_{ci} - j\omega_1)G_{\mathrm{Fi}}(\omega-\omega_1) \\ G_u = G_{\mathrm{Fu}}(\omega-\omega_1) \end{cases} \tag{28}$$

where k denotes the ratio of bandwidth reduction. When f_{Fi} and f_{Fu} meet the constraints of (26) and (27), k=1, otherwise 0<k<1.

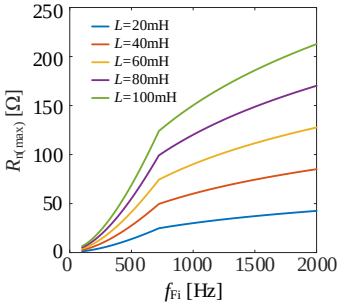

Fig. 5. Relationship between maximum negative damping and LPF bandwidth under different arm inductances (T_d=200μs).

Since the LPF is applied in the dq frame, the frequency of LPF transfer function in (28) is shifted by ω_1 through the Park transformation.

The relationship among MMC damping, LPF bandwidth and dynamic performance is presented in Fig. 4, where the gains in (28) are adopted in this example and MMC with different delay time is distinguished by color. As mentioned above, the LPF bandwidth needs to be reduced for suppression of the negative damping. For MMC with a specific delay time, Fig. 4(a) shows the decreasing process of maximum negative damping $R_{n(max)}$ as LPF bandwidth f_{Fi} gradually reduces from 2000Hz, which is obtained by the numerical calculation. When f_{Fi} is designed highly enough that meets the constraint of (26), control parameters are kept unchanged, so that the control bandwidth f_{ci} stays as shown in Fig. 4(b). The LPF with the decreased f_{Fi} introduces a phase lag ψ at this fixed f_{ci}. It can be seen from Fig. 4(c) that ψ gradually decrease from 0 to -30°. When ψ has reached -30°, further reducing f_{Fi} may affect the stability margin of the control loop. Therefore, f_{ci} has to be reduced in equal proportion with f_{Fi}, ensuring that ψ remains at -30°, as presented in Fig. 4(b) and (c). Fig. 4(a) indicates that $R_{n(max)}$ is suppressed more significantly at this stage. This is due to the fact that in addition to the suppression effect of LPF, the decline of control bandwidth also reduces the voltage and current gains (i.e., k in Eq. (28) is less than one). Fig. 4 (d) gives the relationship between f_{Fi} and f_{Fu}, from which f_{Fu} can be selected after the f_{Fi} is obtained according to the design of negative damping or control bandwidth. Fig. 4 also shows that f_{ci} will rise up with the decrease of delay time T_d, and for the same $R_{n(max)}$, the MMC with smaller T_d can obtain higher control bandwidth.

On the other hand, although the MMC in Fig. 4 takes the 100mH arm inductance as an example, above analysis is applicable to the MMC with any parameter. This is because, according to (17) and (23), L_{eq} can be extracted from $|G_i|$ and $|G_u|\omega L_{eq}\sin\theta_1$, and then it is found that the MMC damping is directly proportional to the arm inductance. Fig. 5 shows the effects of different arm inductance on negative damping, where the analysis results vary linearly with respect to L. Therefore, the negative damping under different inductances can be easily obtained based on the inductance ratio, which also implies the universality of the proposed analysis process.

B. LPF and Damper Joint Design for HFR Suppression

In order to completely eliminate the risk of HFR no matter how the grid impedance changes, the passive damper has to be added to ensure that the high-frequency net damping of the

system always holds positive. There are two types of dampers: series and parallel, in which the series one is inconvenient on installation and maintenance due to the requirement of disconnecting the power line. Therefore, the parallel damper would be discussed in this paper. A simple parallel damper consists of a resistor in series with an *LC* parallel resonant tank [17], in which the resonant tank is used to block the fundamental-frequency current to reduce the loss, and the resistor acts on the high-frequency range to increase the system damping. The system would completely avoid HFR only when the damping added by this resistance exceeds the MMC maximum negative damping generated. Therefore, the damper resistance needs to be designed jointly with the MMC LPF.

Noted that the damping provided by the parallel damper for the grid is not equal to the resistance value, which is different from the series damper. Assuming that the damper resistance R_d is connected in parallel with the grid impedance ($Z_g \approx jX_g$), the damping of the total impedance is

$$\mathrm{Re}\left(\frac{R_d Z_g}{R_d+Z_g}\right)\approx \mathrm{Re}\left(\frac{R_d X_g^2+jR_d^2 X_g}{R_d^2+X_g^2}\right)=\frac{R_d}{R_d^2/X_g^2+1}. \quad (29)$$

To ensure that this damping is always greater than the MMC maximum negative damping $R_{n(max)}$, we have

$$\frac{R_d}{R_d^2/X_g^2+1}\ge R_{n(max)} \Rightarrow \frac{R_{n(max)}}{X_g^2}R_d^2-R_d+R_{n(max)}\le 0. \quad (30)$$

This inequality has a solution only when $R_{n(max)} \le 0.5X_g$ holds. Obviously, the smaller $R_{n(max)}$ is, the more stable the system is, but the smaller $R_{n(max)}$ needs to sacrifice more control bandwidth. Therefore, selecting the critical value, that is $R_{n(max)}=0.5X_g$, is recommended to maintain the MMC dynamic performance as much as possible. On the other hand, in order to make the design result applicable to any grid impedance, the minimum grid impedance $X_{g(min)}$ is considered, substituting which into (30) we have

$$\begin{cases} R_{n(max)} = 0.5X_{g(min)} \\ R_d = X_{g(min)} \end{cases}. \quad (31)$$

Avoiding knowing the exact grid impedance, in this paper, the amplitude of MMC impedance where the negative damping first appears is regarded as $X_{g(min)}$ that may cause HFR. This is because the grid impedance less than this value will no longer intersect with the MMC impedance as the MMC impedance increases continuously in the high-frequency range. After obtaining $X_{g(min)}$, the allowed $R_{n(max)}$ and R_d would be calculated by (31), and the corresponding voltage and current LPF bandwidths can be founded in Fig. 4.

The above joint design can not only realize HFR suppression regardless of the grid impedance variation, but also avoid LPF from deteriorating the control bandwidth to the greatest extent, which provides theoretical support for addressing HFR in MMC-HVDC system. In section V, this joint design method will be demonstrated in detail.

C. HFR Suppression without damper

Although dampers are recommended in solving HFR problems, there is still a situation that MMC stations have been built without enough space for additional dampers. In this case, it is impossible for MMC to completely avoid HFR under arbitrary grid impedance. As a compromise, the frequency of

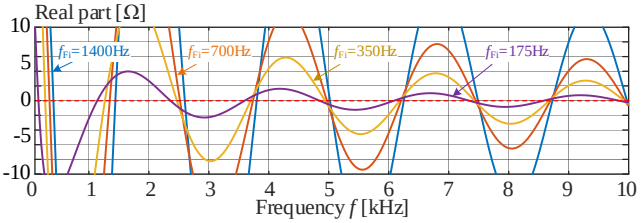

(a) MMC damping with different LPF bandwidth (T_d=400μs).

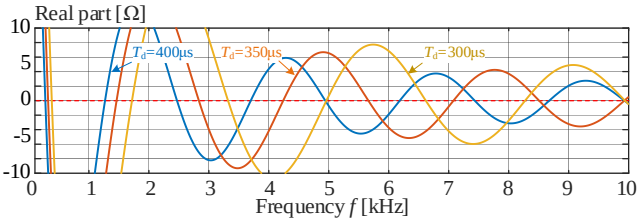

(b) MMC damping with different delay time T_d (f_{Fi}=350Hz).

Fig. 6. Influence of T_d and LPF on the negative damping frequency range.

the MMC negative damping needs to be adjusted to prevent from falling in the potential HFR risk zone.

The HFR risk zone, that is, the possible frequency range where the MMC impedance intersects the capacitive segments of the grid impedance, can be estimated by the proposed UHFIM. The focus of this estimation is to find the variation boundary of MMC impedance. Fig. 3 has shown that the MMC impedance may vary dramatically at high frequencies because $|G_u|$ is close to 1. Fortunately, the addition of LPF can suppress the change of impedance amplitude by attenuating $|G_u|$. It is assumed that $|G_u|$ at the frequency of capacitive grid impedance has been suppressed below ε. Based on this assumption, the amplitude of the MMC impedance satisfies

$$|Z_{ac}|=\left|j\omega L_{eq}+\frac{|G_i|e^{j\theta_2}/\varepsilon+j\omega L_{eq}}{e^{j\theta_1}/\varepsilon-1}\right|=\frac{1}{\varepsilon}\left|\frac{j\omega L_{eq}e^{j\theta_1}+|G_i|e^{j\theta_2}}{e^{j\theta_1}/\varepsilon-1}\right|. \quad (32)$$

According to the triangle inequality, the boundary of MMC impedance in high-frequency range can be estimated as

$$\frac{1}{\varepsilon}\frac{\left|j\omega L_{eq}e^{j\theta_1}+|G_i|e^{j\theta_2}\right|}{1/\varepsilon+1}\le|Z_{ac}|\le\frac{1}{\varepsilon}\frac{\left|j\omega L_{eq}e^{j\theta_1}+|G_i|e^{j\theta_2}\right|}{1/\varepsilon-1} \quad (33)$$

$$\frac{1}{1+\varepsilon}\left(\omega L_{eq}-|G_i|\right)\le|Z_{ac}|\le\frac{1}{1-\varepsilon}\left(\omega L_{eq}+|G_i|\right). \quad (34)$$

The frequency range of the intersection area between the boundary (34) and all possible capacitive segments of the grid impedance would be the HFR risk zone.

On the other hand, after obtaining the HFR risk zone, the next step is to change the frequency range of MMC negative damping. According to Eq. (17), one main factor that affects the distribution of negative damping is the phase angle ($T_d\omega$, φ_i and φ_u) which can shift the position of the zero-crossing point of damping. Among them, φ_i and φ_u introduced by LPF is limited, especially in the high-frequency range (e.g., the first-order LPF can only introduce a 90° phase shift at most). Fig. 6(a) have presented the MMC damping with different LPF bandwidth. When the bandwidth of LPF reduces from 1400Hz to 175Hz, the zero-crossing point of damping moves no more than 300Hz, which shows the limitation of the influence of LPF on the negative damping. On the contrary, the phase lag introduced by the time delay is directly proportional to frequency (i.e., $T_d\omega$). With the increase of frequency, the phase lag would be infinite.

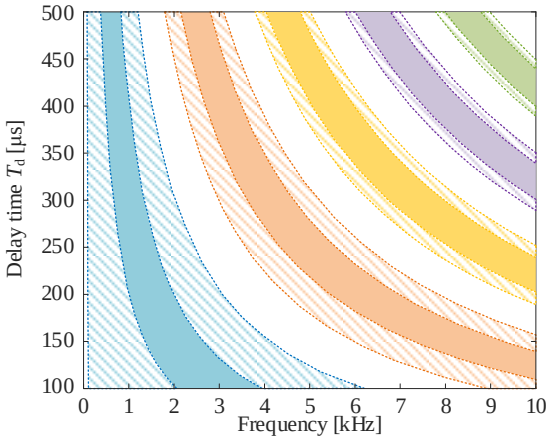

Fig. 7. Relationship between MMC negative damping range and delay time.

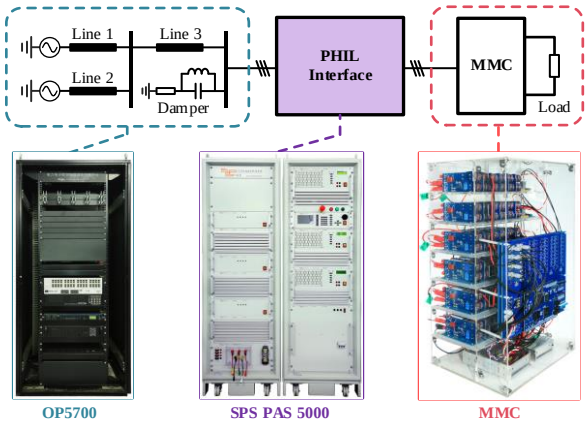

Fig. 8. Experimental platform.

As a result, the adjustment of T_d can significantly change the distribution frequency of negative damping. Fig. 6(b) presents the MMC damping with the adjustment of T_d from 400μs to 300μs. Obviously, changing the time delay greatly moves the frequency range of damping. Recording the zero-crossing point of damping under different delay and LPF bandwidth leads to Fig. 7. The color area in this figure denotes the MMC frequency range with negative damping, and when LPF bandwidth is adjusted, the boundary of this range is changing in the shadow with hatching line. It can be seen that the adjustment of T_d results in a variation range of thousands of Hertz with regard to the frequency with negative damping, which may help the HFR risk zone avoid touching the MMC negative damping. In practice, the system can get out of the HFR risk by mainly changing T_d, and the adjustment of LPF is used as an auxiliary means. The case study of using this method to suppress HFR will be demonstrated in section V.

V. Verification and Case Study

The UHFIM and HFR suppression method proposed in this paper are verified by the power hardware-in-the-loop (PHIL) based experiment. The structure of the experimental platform is shown in Fig. 8, where a downscaled physical prototype of MMC (C=2.04 mF, L=4.2 mH, N=6) is connected with the grid through power amplifier (SPS PAS 5000). The grid is realized by the real-time simulator (OP5700) which consists of a three-terminal grid with MMC connected to one end. The

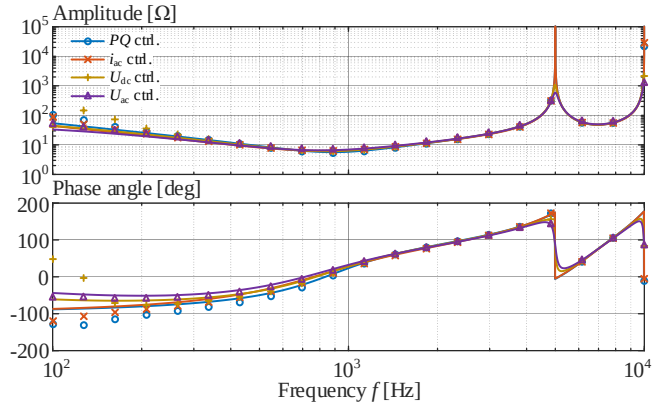

Fig. 9. Frequency sweep of MMC under different control strategies.

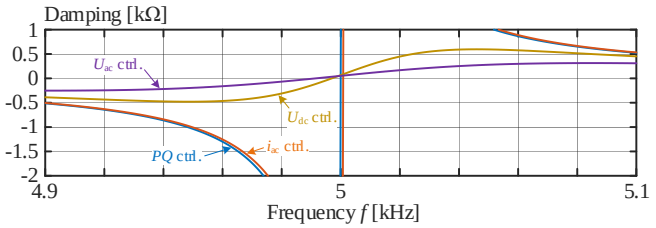

Fig. 10. Comparison of MMC damping under different control strategies.

π-model is adopted to simulate the impedance of power line, where the capacitance segments are set deliberately to intersect with MMC impedance for demonstrating the HFR suppression method.

A. Verification of MMC UHFIM

The frequency sweep is firstly presented in Fig. 9 to verify the accuracy of the proposed UHFIM under different operation mode. Impedances under different control strategies including power control, ac current control, dc voltage control and ac voltage control are colored in blue, orange, yellow and purple, respectively. The theoretical impedance calculated by UHFIM is drawn by solid lines, while the data obtained by simulation frequency sweep is marked as scattered points. The MMC is operating without LPF and the control delay is 200μs. The K_{iac} of MMC are set as 5.5 for getting around 420Hz current control bandwidth and 60° phase margin. Although there is a small deviation at low frequency, in the high-frequency range where the resonant peak and negative damping exist, the swept data fully fits the impedance curve drawn by UHFIM (16), indicating that the proposed model has sufficient accuracy to study HFR issues under different control strategies. Fig. 10 further compares the MMC high-frequency damping under different control strategies. It can be seen that both power control and ac current control will produce infinite negative damping because G_u is close to 1, among which the negative damping under power control is slightly greater due to the greater G_i introduced by the controller. Under dc voltage control, G_u is not equal to 1, so the negative damping in high frequency is limited as shown in yellow curve. The lowest risk of HFR occurs in ac voltage control, where the controller can not only weaken G_u to avoid infinite negative damping, but also have the smallest G_i. The results shown in Fig. 10 are consistent with the discussion in Section III-C where the influence of different control strategies on negative damping is analyzed based on the UHFIM.

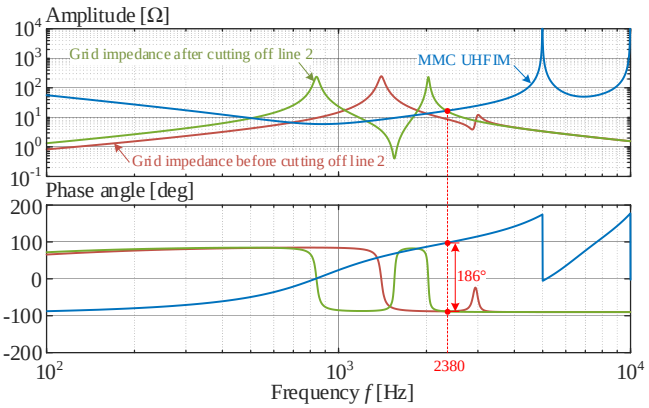

Fig. 11. Stability analysis based on UHFIM under the power control.

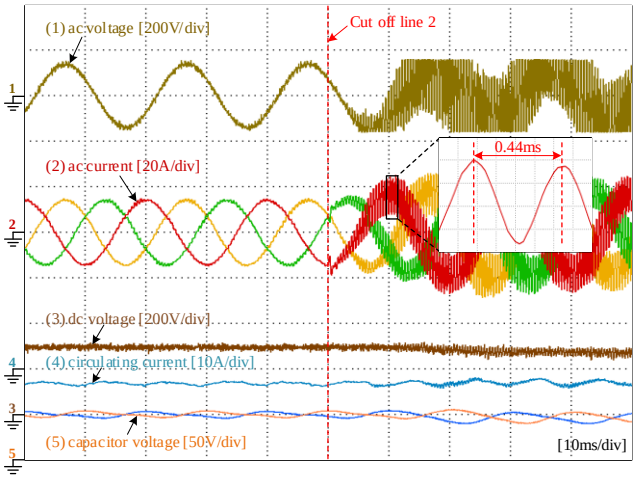

Fig. 12. Experiential waveforms of MMC without LPF.

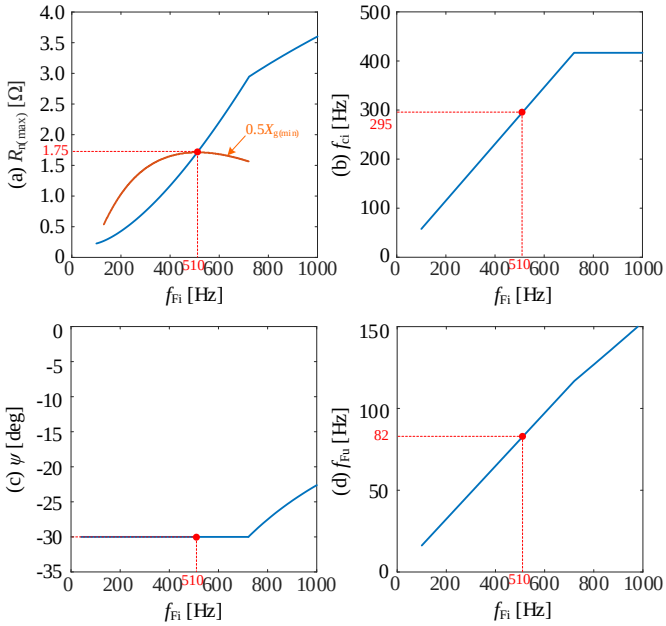

Fig. 13. Schematic diagram of designing R_d according to $R_{n(max)}$ and $X_{g(min)}$.

On the other hand, the red and green curves in Fig. 11 respectively represent grid impedances with and without line 2 drawn in Fig. 8. It can be seen that after cutting off line 2, MMC will have an unstable intersection with the grid impedance near 2380Hz, where the phase margin is -6°. This unstable

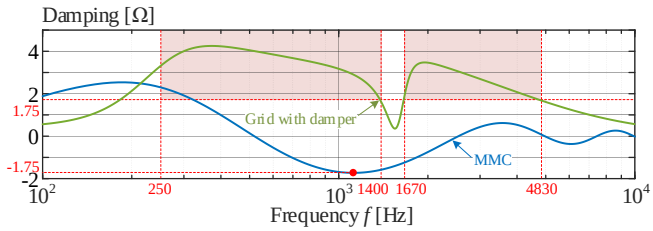

Fig. 14. Damping of the MMC and the grid after adding the damper.

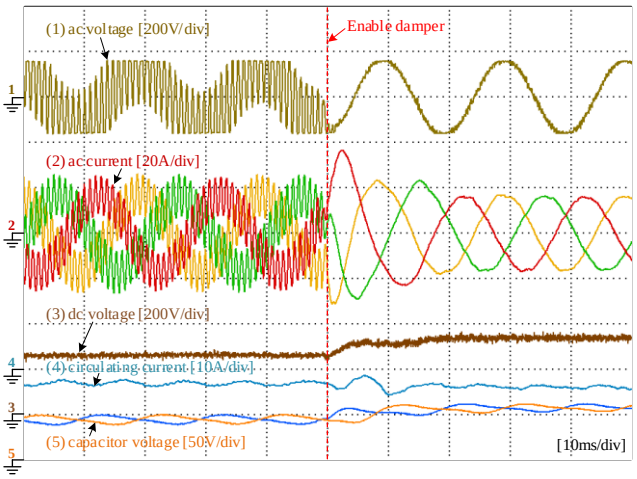

Fig. 15. Experiential waveforms of MMC with damper.

phenomenon is confirmed by the experimental results in Fig. 12. Waveforms show that the MMC operates stably with a power of 3kW at the beginning. When line 2 is cut off, the system appears significant HFR with the oscillation frequency around 2273Hz, which is close to the predicted value and verifies the correctness of the UHFIM in stability analysis. Besides, it can be found that HFR is mainly concentrated on the ac side, while the voltage and current on dc side as well as capacitor voltage are comparatively calm, indicating that the MMC dc and ac sides are decoupled in high-frequency range. This confirms the assumption in section II that the high-frequency coupling between ac and dc sides can be ignored in the derivation of the MMC high-frequency model.

B. HFR Suppression with Damper

This part aims to demonstrate the effectiveness of the proposed joint design method for HFR suppression. According to (31), the allowed MMC maximum negative damping R_d needs to be determined firstly by the minimum grid impedance $X_{g(min)}$, which is considered as the MMC impedance where the negative damping first appears. Fig. 13 shows the relationship among $R_{n(max)}$, LPF bandwidths and current control bandwidth under experimental parameters in blue color. In addition, the $0.5X_{g(min)}$ in (31) is also plotted in Fig. 13(a) as the orange curve. The intersection of $R_{n(max)}$ and $0.5X_{g(min)}$ is selected in this paper where the damper can just offset the MMC maximum negative damping (i.e., $R_{n(max)}$=$0.5X_{g(min)}$=1.75Ω), and 510Hz current LPF and 82Hz voltage LPF are needed. At this point, the current control bandwidth is expected as 295Hz, substituting which into (20) can get around 69° phase margin without LPF. Considering that LPF introduces -30° phase lag at f_{ci}, the actual phase margin of MMC is about 39°. The damper resistance R_d can be calculated as 3.5Ω through (31). In this experiment, the resonant tank of the damper is composed of

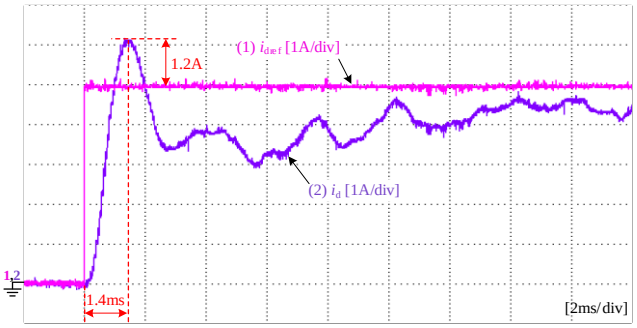

Fig. 16. Dynamic waveform of MMC d-axis current.

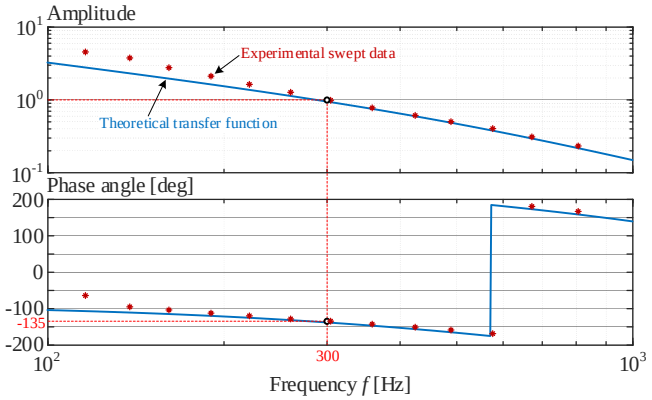

Fig. 17. Experimental frequency sweep of MMC current loop.

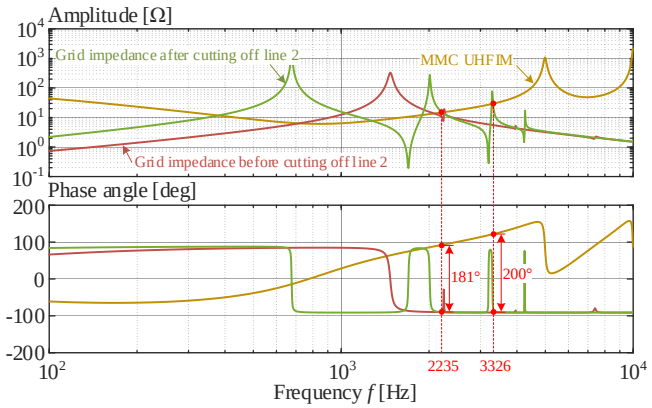

Fig. 18. Stability analysis based on UHFIM under the dc voltage control.

50mH inductance and 202μF capacitance, so as to obtain the parallel resonant frequency of 50Hz to block the fundamental frequency current.

The blue line in Fig. 14 shows the MMC damping after configuring LPF. The second-order voltage and first-order current LPFs ensure that the MMC damping converges to zero with increase of frequency, and the reasonable bandwidth of LPF make the maximum negative damping around 1.75Ω, which is consistent with the design goal. The damping of the grid with damper is also plotted in this figure in green color. It can be seen that the damper adds at least 1.75Ω positive damping to the frequency range where the amplitude of the original grid impedance shown in Fig. 11 exceeds $X_{g(min)}$, and it is also presented as a red shaded area in Fig. 14. The system net damping is positive in these areas and MMC can avoid HFR.

Fig. 15 proves the correctness of the proposed joint design method through experiments. At the beginning, the MMC only with the LPF still oscillates because the original damping of the

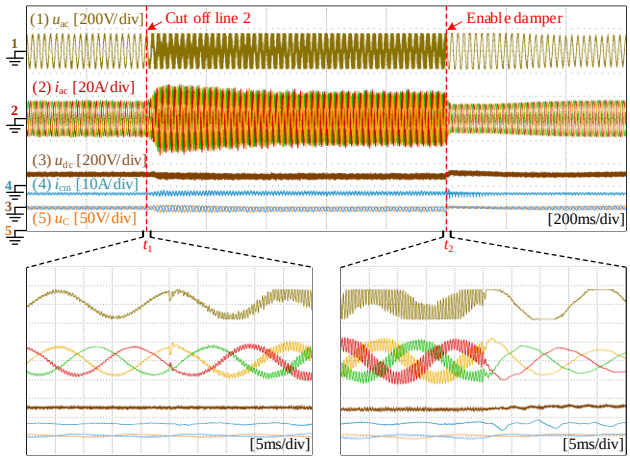

(a) Experiential waveforms

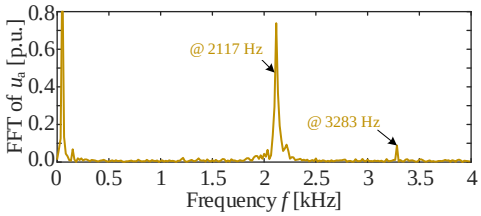

(b) FFT result of MMC ac voltage

Fig. 19. Experiential results under the dc voltage control.

power grid is not enough to offset the negative damping of MMC. After enabling the designed damper, the HFR is rapidly suppressed and the system returns to stability. On the other hand, according to control theory [25], the system with f_{ci} of 295Hz and γ_i of 39° corresponds to around 1.56ms peak time and 28.6% overshoot. To verify the influence of joint design method on dynamic performance, Fig. 16 presents the dynamic waveform of MMC d-axis current, where the reference of the current is step up from 15A to 20A. The 1.4ms peak time and 24% overshoot (1.2A) can be observed in this dynamic current, which is close with the predicted values. Furthermore, the frequency sweep of the current control loop has been done experimentally, in which 2A perturbation current with different frequencies are injected into the current reference, and the Bode plot of the current loop transfer function can be obtained as Fig. 17. The experimental swept data is consistent with the theoretical curve, and f_{ci} is around 300Hz which confirms the designed value. The slight error in low frequency is due to the fact that the proposed UHFIM ignores the harmonic coupling of MMC, which is relatively small and will not affect the HFR analysis in this paper.

In order to verify the universality of the proposed method under different control strategy, grid impedance and oscillation frequency, the experiment with the dc voltage regulating MMC and connecting with more complex grid impedance is presented. Impedances of MMC and grid have been shown in Fig. 18, where the power line consists of more π-sections, resulting in multiple resonant points in the grid impedance after line 2 is cut off. Two unstable high-frequency intersections can be found in this case, which are at 2235Hz and 3326Hz, respectively. The experimental waveforms given in Fig. 19 (a) confirm the conclusion of impedance analysis, where line 2 is cut off at t_1, and the originally stable system begins to oscillate. The FFT result in Fig. 19 (b) shows that the oscillation contains 2217 and

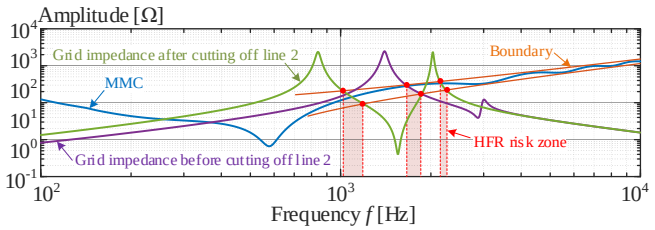

Fig. 20. Risk zone estimation based on UHFIM.

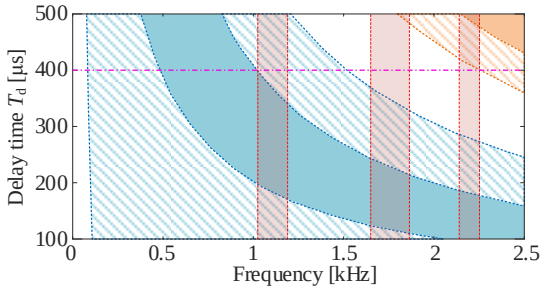

Fig. 21. Schematic of avoiding risk zone by adjusting delay time.

3283Hz components at the same time, which is close to the theoretical prediction. At t_2, the inserting of damper makes the system back to stable, showing that the proposed unified model and joint design method can be used to analyze and suppress HFR under different control strategies and grid conditions.

C. HFR Suppression by Adjusting Delay Time

The effectiveness of the HFR suppression method without damper is further verified in this part. Substituting experimental parameters into (34), the boundary of MMC impedance can be obtained and shown as the orange curves in Fig. 20, where the amplitude of MMC high-frequency impedance varies within this boundary range, confirming the accuracy of Eq. (34). By intersecting the boundary with capacitive segments of all possible grid impedances, the frequency ranges with HFR risk are obtained as (1025, 1190) Hz, (1650, 1864) Hz and (2140, 2252) Hz, which are also marked in Fig. 20 in red color. Projecting these risk zones into Fig. 7 leads to Fig. 21. Obviously, HRF risk cannot be avoided by just changing LPF bandwidth under delay of 200μs. Only when the delay increases to 400μs, the risk zone may jump out of the MMC negative damping range. Fig. 22 shows the experimental waveform with the modified delay time. It can be seen that the system can keep stable when line 2 is cut off, which verifies the effectiveness of the proposed HFR suppression method without damper.

VI. Conclusions

The UHFIM, which can reflect the MMC high-frequency characteristics under different control strategies in a unified form, is proposed in this paper. Based on this model, the constraint of LPF order on the convergence of MMC high-frequency damping is revealed. It shows that at least second-order voltage LPF and first-order current LPF are needed to converge the MMC high-frequency negative damping to zero. Also, the UHFIM points out that the power control is the worst case with HFR risk while the ac voltage control is the opposite. By analyzing the relationship among MMC maximum negative damping, LPF bandwidth and MMC dynamic performance, this paper proposes a joint design

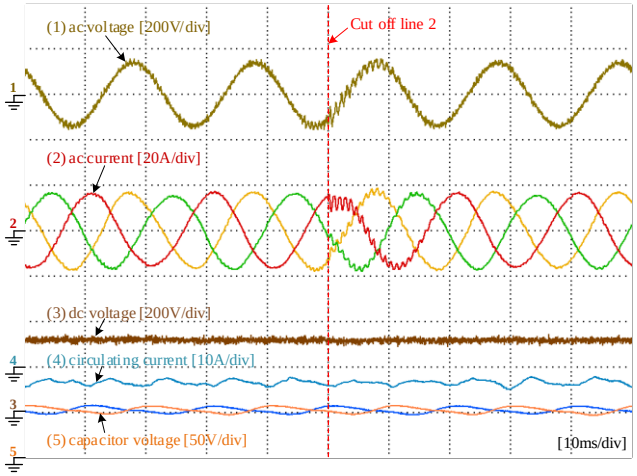

Fig. 22. Experimental waveform of MMC with modified delay time.

method for LPF and passive damper, which can eliminate the HFR risk no matter how the grid impedance changes, and deteriorate the control bandwidth as little as possible. Besides, for the situation that MMC stations have been built without enough space for additional dampers, this paper also develops an alternative HFR suppression method by adjusting the delay time, where the frequency of the MMC negative damping range can be moved to avoid falling in the potential HFR risk zone. The model, analysis and HFR suppression methods proposed in this paper are of universality, and would be helpful for solving HFR issue in various control strategies and grid environments.

Appendix

This part gives an example to derive and simplify the MMC impedance under the ac current control. The control strategy includes current reference (i_{dref}, i_{qref}), PI controller, dq decoupling link ($0.5\omega_1 L$), ac voltage feedforward link (u_d, u_q), Park and inverse Park transformation, and the influence of PLL. Along the block diagram shown in Fig. 2 (d), the expressions of ac current and voltage in dq frame can be obtained as

$$\begin{cases} \tilde{\mathbf{u}}_d = \mathbf{T}_{d+}e^{-j\omega T_d}\tilde{\mathbf{u}}_{ac} + \mathbf{u}'_{d+}\mathbf{G}_{PLL}e^{-j\omega T_d}\tilde{\mathbf{u}}_{ac} \\ \tilde{\mathbf{u}}_q = \mathbf{T}_{q+}e^{-j\omega T_d}\tilde{\mathbf{u}}_{ac} + \mathbf{u}'_{q+}\mathbf{G}_{PLL}e^{-j\omega T_d}\tilde{\mathbf{u}}_{ac} \end{cases} \tag{a1}$$

$$\begin{cases} \tilde{\mathbf{i}}_d = \mathbf{T}_{d+}e^{-j\omega T_d}\tilde{\mathbf{i}}_{ac} + \mathbf{i}'_{d+}\mathbf{G}_{PLL}e^{-j\omega T_d}\tilde{\mathbf{u}}_{ac} \\ \tilde{\mathbf{i}}_q = \mathbf{T}_{q+}e^{-j\omega T_d}\tilde{\mathbf{i}}_{ac} + \mathbf{i}'_{q+}\mathbf{G}_{PLL}e^{-j\omega T_d}\tilde{\mathbf{u}}_{ac} \end{cases} \tag{a2}$$

where $\mathbf{T}_{d+}$ and $\mathbf{T}_{q+}$ in the first term represent the frequency shift effect of Park transform on voltage or current signal, and the second term represents the influence of ac voltage perturbation on the Park transformation through PLL. $\mathbf{u}'_{d+}$, $\mathbf{u}'_{q+}$, $\mathbf{i}'_{d+}$ and $\mathbf{i}'_{q+}$ are steady-state voltages and currents introduced by PLL, which has been strictly derived in [19]. Combining these dq signals according to Fig. 2 (d), we have

$$\begin{cases} \tilde{\mathbf{m}}_{dmd} = \left(Nu_{CN}\right)^{-1}\left[\mathbf{G}_{iac}\left(-\tilde{\mathbf{i}}_{dref} + \tilde{\mathbf{i}}_d\right) + \omega_1 L_{eq}\tilde{\mathbf{i}}_q + \tilde{\mathbf{u}}_d\right] \\ \tilde{\mathbf{m}}_{dmq} = \left(Nu_{CN}\right)^{-1}\left[\mathbf{G}_{iac}\left(-\tilde{\mathbf{i}}_{qref} + \tilde{\mathbf{i}}_q\right) - \omega_1 L_{eq}\tilde{\mathbf{i}}_d + \tilde{\mathbf{u}}_q\right] \end{cases}. \tag{a3}$$

These modulation indexes in dq frame can be transformed by the inverse Park transform, gives

$$\tilde{\mathbf{m}}_{dm} = \mathbf{T}_{d-}\tilde{\mathbf{m}}_{dmd} + \mathbf{T}_{q-}\tilde{\mathbf{m}}_{dmq} + \mathbf{m}'_{dmdq-}\mathbf{G}_{PLL}\tilde{\mathbf{u}}_{ac} \tag{a4}$$

where $\mathbf{T}_{d-}$ and $\mathbf{T}_{q-}$ represent the frequency shift effect of inverse Park transform. Substituting (a1)-(a3) into (a4), the modulation index in HSS is obtain as

$$\tilde{\mathbf{m}}_{dm}=\frac{1}{Nu_{CN}}\begin{bmatrix}-\left(\mathbf{T}_{d-}\mathbf{G}_{iac}\tilde{\mathbf{i}}_{dref}+\mathbf{T}_{q-}\mathbf{G}_{iac}\tilde{\mathbf{i}}_{qref}\right)\\+\left(\mathbf{T}_{d-}\mathbf{G}_{iac}\mathbf{T}_{d+}+\mathbf{T}_{q-}\mathbf{G}_{iac}\mathbf{T}_{q+}\right)e^{-j\omega T_d}\tilde{\mathbf{i}}_{ac}\\+\omega_1 L_{eq}\left(\mathbf{T}_{d-}\mathbf{T}_{q+}-\mathbf{T}_{q-}\mathbf{T}_{d+}\right)e^{-j\omega T_d}\tilde{\mathbf{i}}_{ac}\\+\left(\mathbf{T}_{d-}\mathbf{T}_{d+}+\mathbf{T}_{q-}\mathbf{T}_{q+}\right)e^{-j\omega T_d}\tilde{\mathbf{u}}_{ac}\\+\left(\mathbf{T}_{d-}\mathbf{G}_{iac}\mathbf{i}'_{d+}+\mathbf{T}_{q-}\mathbf{G}_{iac}\mathbf{i}'_{q+}\right)\mathbf{G}_{PLL}e^{-j\omega T_d}\tilde{\mathbf{u}}_{ac}\\+\omega_1 L_{eq}\left(\mathbf{T}_{d-}\mathbf{i}'_{q+}-\mathbf{T}_{q-}\mathbf{i}'_{d+}\right)\mathbf{G}_{PLL}e^{-j\omega T_d}\tilde{\mathbf{u}}_{ac}\\+\left(\mathbf{T}_{d-}\mathbf{u}'_{d+}+\mathbf{T}_{q-}\mathbf{u}'_{q+}\right)\mathbf{G}_{PLL}e^{-j\omega T_d}\tilde{\mathbf{u}}_{ac}\\+Nu_{CN}\mathbf{m}'_{dmdq-}\mathbf{G}_{PLL}e^{-j\omega T_d}\tilde{\mathbf{u}}_{ac}\end{bmatrix}. \quad \text{(a5)}$$

The first four rows in the equation correspond to dq current reference signal, ac current feedback control, dq current decoupling and ac voltage feedforward, respectively. The fifth to seventh rows are introduced by PLL and Park transformation while the last row is introduced by inverse Park transformation.

In the high-frequency range, the PLL and the integral link in the PI controller can be ignored as their bandwidth or turning frequency usually does not exceed 100 Hz. Removing the terms corresponding to PLL and integral link from (a5), we have

$$\tilde{\mathbf{m}}_{dm}\approx\frac{1}{Nu_{CN}}\begin{bmatrix}-\left(\mathbf{T}_{d-}K_{iac}\tilde{\mathbf{i}}_{dref}+\mathbf{T}_{q-}K_{iac}\tilde{\mathbf{i}}_{qref}\right)\\+\left(\mathbf{T}_{d-}K_{iac}\mathbf{T}_{d+}+\mathbf{T}_{q-}K_{iac}\mathbf{T}_{q+}\right)e^{-j\omega T_d}\tilde{\mathbf{i}}_{ac}\\+\omega_1 L_{eq}\left(\mathbf{T}_{d-}\mathbf{T}_{q+}-\mathbf{T}_{q-}\mathbf{T}_{d+}\right)e^{-j\omega T_d}\tilde{\mathbf{i}}_{ac}\\+\left(\mathbf{T}_{d-}\mathbf{T}_{d+}+\mathbf{T}_{q-}\mathbf{T}_{q+}\right)e^{-j\omega T_d}\tilde{\mathbf{u}}_{ac}\end{bmatrix} \quad \text{(a6)}$$

where $\mathbf{T}_{d+}$, $\mathbf{T}_{q+}$, $\mathbf{T}_{d-}$ and $\mathbf{T}_{q-}$ can be is further simplified according to [19], leading to

$$\begin{aligned}\tilde{\mathbf{m}}_{dm}=\frac{1}{NU_{CN}}\Big\{&-\mathbf{T}_{d-}K_{iac}\tilde{\mathbf{i}}_{dref}-\mathbf{T}_{q-}K_{iac}\tilde{\mathbf{i}}_{qref}+\mathbf{E}^{s}_{\pm}e^{-j\omega T_d}\tilde{\mathbf{u}}_{ac}\\&+\left[K_{iac}\mathbf{E}^{s}_{\pm}+j\left(-\mathbf{E}^{s}_{+}+\mathbf{E}^{s}_{-}\right)\omega_1 L_{eq}\right]e^{-j\omega T_d}\tilde{\mathbf{i}}_{ac}\Big\}\end{aligned} \quad \text{(a7)}$$

which is Eq. (4) in the section II-B.

REFERENCES

[1] Y. Chi, B. Tang, J. Hu et al., "Overview of mechanism and mitigation measures on multi-frequency oscillation caused by large-scale integration of wind power," *CSEE Journal of Power and Energy Systems*, vol. 5, no. 4, pp. 433-443, Dec. 2019.

[2] J. Wang, J. D. Yan, L. Jiang et al., "Delay-dependent stability of single-loop controlled grid-connected inverters with LCL filters," *IEEE Transactions on Power Electronics*, vol. 31, no. 1, pp. 743-757, Jan. 2016.

[3] X. Wang, F. Blaabjerg, P. C. Loh, "Grid-current- feedback active damping for LCL resonance in grid-connected voltage-source converters," *IEEE Transactions on Power Electronics*, vol. 31, no. 1, pp. 213-223, Jan. 2016.

[4] G. Feng, Z. Ye, Y. Xia, et al., "High frequency resonance suppression strategy of three-phase four-wire split capacitor inverter connected to parallel compensation grid", *Energies*. vol. 15, no. 4, pp. 1486.

[5] D. Yang, X. Ruan, H. Wu, "A real-time computation method with dual sampling mode to improve the current control performance of the LCL-type grid- connected inverter," *IEEE Transactions on Industrial Electronics*, vol. 62, no. 7, pp. 4563-4572, July 2015.

[6] F. Wang, K. Liu, S. Zhu, et al., "High-frequency resonance analysis and stabilization control strategy of MMC based on eigenvalue method," *IEEE Access*, vol. 9, pp. 16305-16315, 2021.

[7] C. Dong, S. Yang, H. Jia et al., "Padé-based stability analysis for a modular multilevel converter considering the time delay in the digital control system," *IEEE Transactions on Industrial Electronics*, vol. 66, no. 7, pp. 5242-5253, July 2019.

[8] C. Wang, L. Xiao, H. Jiang et al., "Analysis and compensation of the system time delay in an MMC system," *IEEE Transactions on Power Electronics*, vol. 33, no. 11, pp. 9923-9936, Nov. 2018.

[9] C. Zou, H. Rao, S. Xu et al., "Analysis of resonance between a VSC-HVDC converter and the ac grid," *IEEE Transactions on Power Electronics*, vol. 33, no. 12, pp. 10157-10168, Dec. 2018.

[10] Y. Li, T. An, D. Zhang, et al., "Analysis and suppression control of high frequency resonance for MMC-HVDC system," *IEEE Transactions on Power Delivery*, vol. 36, no. 6, pp. 3867-3881, Dec. 2021.

[11] X. Guo, B. Yuan, X. Li et al., "Research on the high frequency oscillation of MMC-HVDC integrated into renewable energy system," in *Proc. 2021 IEEE Southern Power Electronics Conference (SPEC)*, Kigali, Rwanda, 2021, pp. 1-6.

[12] Y. Li, H. Pang, M. Kong, et al., "Compensation control and parameters design for high frequency resonance suppression of MMC-HVDC system," *CSEE Journal of Power and Energy Systems*, vol. 7, no. 6, pp. 1161-1175, Nov. 2021.

[13] B. Pang, H. Nian, Y. Xu, "Mechanism analysis and damping method for high frequency resonance between VSC-HVDC and the wind farm" *IEEE Transactions on Energy Conversion*, vol. 36, no. 2, pp. 984-994, June 2021.

[14] J. Man: J. Man, L. Chen, et al., "Mitigating high-frequency resonance in MMC-HVDC systems using adaptive notch filters" *IEEE Transactions on Power Systems*, vol. 37, no. 3, pp. 2086-2096, May 2022.

[15] J. Zhu, J. Hu, L. Lin, et al., "High-frequency oscillation mechanism analysis and suppression method of VSC-HVDC," *IEEE Transactions on Power Electronics*, vol. 35, no. 9, pp. 8892-8896, Sept. 2020.

[16] K. Ji, W. Chen, X. Wu et al., "High frequency stability constraints based MMC controller design applying NSGA-III algorithm," *CSEE Journal of Power and Energy Systems*, to be published.

[17] J. Sun, "Passive Methods to Damp AC Power System Resonance Involving Power Electronics," in *Proc. 2018 IEEE 19th Workshop on Control and Modeling for Power Electronics (COMPEL)*, Padua, Italy, 2018, pp. 1-8.

[18] K. Ji, H. Pang, Z. He, et al., "Active/passive method based hybrid high frequency damping design for MMCs," *IEEE Journal of Emerging and Selected Topics in Power Electronics*, vol. 9, no. 5, pp. 6086-6098, Oct. 2021.

[19] Z. Xu, B. Li, L. Han et al., "A complete HSS-based impedance model of MMC considering grid impedance coupling," *IEEE Transactions on Power Electronics*, vol. 35, no. 12, pp. 12929-12948, Dec. 2020.

[20] Z. Xu, B. Li, S. Li et al., "MMC admittance model simplification based on signal-flow graph," *IEEE Transactions on Power Electronics*, vol. 37, no. 5, pp. 5547-5561, May 2022.

[21] S. Thakur, M. Odavic, Z. Zhu, "Modeling and optimization of low-capacitance half-bridge modular multilevel converters operated with average submodule capacitor voltage control," *IEEE Transactions on Industry Applications*, vol. 57, no. 6, pp. 6131-6144, 2021.

[22] B. Li, Z. Xu, J. Ding et al., "Decoupled modeling and control of the modular multilevel converter," in *Proc. 2018 IEEE Applied Power Electronics Conference and Exposition (APEC)*, 2018, pp. 3275-3280.

[23] J. Sun, I. Vieto, E. V. Larsen, et al., "Impedance-based characterization of digital control delay and its effects on system stability," in *Proc. 2019 20th Workshop on Control and Modeling for Power Electronics (COMPEL)*, Toronto, ON, Canada, 2019, pp. 1-8.

[24] V. Blasko, V. Kaura, "A new mathematical model and control of a three-phase AC-DC voltage source converter," *IEEE Transactions on Power Electronics*, vol. 12, no. 1, pp. 116-123, Jan. 1997.

[25] K. Ogata, *Modern control engineering*, 5th ed. Upper Saddle River: Prentice-Hall, 2010.

Zigao Xu (S'17) received the B.S. degree in electrical engineering from the Taiyuan University of Technology, Taiyuan, China, in 2016, and the M.S. degrees in 2018 from the Harbin Institute of Technology, Harbin, China, where he is currently working toward the Ph.D. degrees.

His current research interests include modeling and control of multilevel converters.

Binbin Li (S'15, M'17, SM'21) received the B.S., M.S., and Ph.D. degrees in electrical engineering from the Harbin Institute of Technology, Harbin, China, in 2010, 2012, and 2017, respectively.

From 2015 to 2016, he was a Visiting Researcher with the Department of Electronic and Electrical Engineering, University of Strathclyde, Glasgow, U.K. He is currently a Professor with the Department of Electrical Engineering, Harbin Institute of Technology, and he has been selected in the Young Elite Scientists Sponsorship Program by China Association for Science and Technology. His research interests include modular power converters, HVDC grid, and MVDC collection/distribution system.

Xiongfei Wang (S'10, M'13, SM'17) received the B.S. degree from Yanshan University, Qinhuangdao, China, in 2006, the M.S. degree from Harbin Institute of Technology, Harbin, China, in 2008, both in electrical engineering, and the Ph.D. degree in energy technology from Aalborg University, Aalborg, Denmark, in 2013.

From 2009 he has been with the Department of Energy, Aalborg University (AAU Energy), where he became an Assistant Professor in 2014, an Associate Professor in 2016, a Professor and Leader of Electronic Power Grid (eGRID) Research Group in 2018. He has also been a part-time Professor at KTH Royal Institute of Technology, Stockholm, Sweden, from 2020. His current research interests include modeling and control of power electronic converters and systems, stability and power quality of power-electronics-dominated power systems, high-power converters.

Dr. Wang serves as Co-Editor-in-Chief for the IEEE TRANSACTIONS ON POWER ELECTRONICS and as Associate Editor for the IEEE JOURNAL OF EMERGING AND SELECTED TOPICS IN POWER ELECTRONICS (JESTPE). He has received 9 Prize Paper Awards in the IEEE Transactions and conferences, the 2016 AAU Talent for Future Research Leaders, the 2018 Richard M. Bass Outstanding Young Power Electronics Engineer Award, the 2019 IEEE PELS Sustainable Energy Systems Technical Achievement Award, the 2020 IEEE PES Prize Paper Award, the 2020 JESTPE Star Associate Editor Award, the 2022 Isao Takahashi Power Electronics Award, and the Highly Cited Researcher in the Web of Science from 2019.

Frede Blaabjerg (S'86–M'88–SM'97–F'03) was with ABB-Scandia, Randers, Denmark, from 1987 to 1988. From 1988 to 1992, he got the PhD degree in Electrical Engineering at Aalborg University in 1995. He became an Assistant Professor in 1992, an Associate Professor in 1996, and a Full Professor of power electronics and drives in 1998. From 2017 he became a Villum Investigator. He is honoris causa at University Politehnica Timisoara (UPT), Romania and Tallinn Technical University (TTU) in Estonia.

His current research interests include power electronics and its applications such as in wind turbines, PV systems, reliability, harmonics and adjustable speed drives. He has published more than 600 journal papers in the fields of power electronics and its applications. He is the co-author of four monographs and editor of ten books in power electronics and its applications.

He has received 32 IEEE Prize Paper Awards, the IEEE PELS Distinguished Service Award in 2009, the EPE-PEMC Council Award in 2010, the IEEE William E. Newell Power Electronics Award 2014, the Villum Kann Rasmussen Research Award 2014, the Global Energy Prize in 2019, and the 2020 IEEE Edison Medal. He was the Editor-in-Chief of the IEEE Transactions on Power Electronics from 2006 to 2012. He has been Distinguished Lecturer for the IEEE Power Electronics Society from 2005 to 2007 and for the IEEE Industry Applications Society from 2010 to 2011 as well as 2017 to 2018. In 2019-2020 he serves a President of IEEE Power Electronics Society. He is Vice-President of the Danish Academy of Technical Sciences too. He is nominated in 2014-2019 by Thomson Reuters to be between the most 250 cited researchers in Engineering in the world.

Dianguo Xu (M'97, SM'12, F'17) received the B.S. degree in Control Engineering from Harbin Engineering University, Harbin, China, in 1982, and the M.S. and Ph.D. degrees in Electrical Engineering from Harbin Institute of Technology (HIT), Harbin, China, in 1984 and 1989 respectively.

In 1984, he joined the Department of Electrical Engineering, HIT as an Assistant Professor. Since 1994, he has been a Professor in the Department of Electrical Engineering, HIT. He was the Dean of School of Electrical Engineering and Automation, HIT, from 2000 to 2010. He is currently the Vice President of HIT. His research interests include renewable energy generation technology, multi-terminal HVDC system based on VSC, power quality mitigation, speed sensorless vector controlled motor drives, high performance servo system. He has published over 600 technical papers.

Prof. Xu is an Associate Editor of the IEEE Transactions on Industrial Electronics, IEEE Transactions on Power Electronics, and the IEEE Journal of Emerging and Selected Topics in Power Electronics. He also serves as Chairman of IEEE Harbin Section.